Stability Analysis of Digital-Controlled Single-Phase Inverter With Synchronous Reference Frame Voltage Control

Yang Han, *Senior Member, IEEE*, Xu Fang, Ping Yang, Congling Wang, Lin Xu, and Josep M. Guerrero, *Fellow, IEEE*

***Abstract*—Stability analysis of single-phase power converters controlled in stationary reference frame is now mature and well developed, by using either linear or nonlinear methods. However, for the single-phase converters with synchronous reference frame (SRF) control loops, little work has been done on the evaluation of the nonlinear approaches for stability analysis. In this paper, the stability of a digital-controlled single-phase voltage-source inverter (VSI) with SRF voltage control loop is investigated from the perspective of nonlinear system. The analysis is based on the discrete-time model defined by the stroboscopic map, which is derived using the state-space averaging (SSA) technique. Furthermore, two different nonlinear analysis methods, the Jacobian matrix method and the Lyapunov exponent method, are adopted to analyze the fast-scale stability and the slow-scale stability of the pulsewidth-modulated (PWM) inverter under variations of control parameters; hence, the stability regions can be obtained. The theoretical results indicate that, for the established stroboscopic models, the Jacobian matrix method and the Lyapunov exponent method are mathematically equivalent, which means that the fast-scale stability and the slow-scale stability of the studied single-phase VSI are consistent, especially under linear load conditions. Experimental results under resistive load, inductive–resistive load, and diode rectifier load conditions are presented to support the theoretical results, which also proves that the discrete-time model plus the Jacobian matrix method or the Lyapunov exponent method is capable to investigate the stability of a converter with SRF control loops accurately.**

***Index Terms*—Jacobian matrix, Lyapunov exponent, nonlinearity, single phase, stroboscopic map, synchronous reference frame (SRF), voltage-source inverter (VSI).**

Manuscript received September 10, 2016; revised January 5, 2017, March 22, 2017, and June 29, 2017; accepted August 17, 2017. Date of publication August 29, 2017; date of current version March 5, 2018. This work was supported by the Sichuan Province Key Research and Development Project under Grant 2017GZ0347. Recommended for publication by Associate Editor Prof. Gerardo Escobar. *(Corresponding author: Josep M. Guerrero.)*

Y. Han, X. Fang, P. Yang, and C. Wang are with the Department of Power Electronics, School of Mechatronics Engineering, University of Electronic Science and Technology of China, Chengdu 611731, China (e-mail: hanyang@uestc.edu.cn; Xulinks@126.com; ping@uestc.edu.cn; wangcl12@163.com).

L. Xu is with the Sichuan Electric Power Research Institute, Sichuan Electric Power Company, Chengdu 610072, China (e-mail: xulinn@163.com).

J. M. Guerrero is with the Department of Energy Technology, Aalborg University, Aalborg 9220, Denmark (e-mail: joz@et.aau.dk).

Color versions of one or more of the figures in this paper are available online at http://ieeexplore.ieee.org.

Digital Object Identifier 10.1109/TPEL.2017.2746743

I. Introduction

SINGLE-PHASE voltage-source inverters (VSIs) are widely used in various industrial fields and play an important role in renewable energy systems, including distributed generations (DGs) and microgrids (MGs) by serving as the interface for single-phase grid or local loads, due to the increasing penetration of renewable energy in recent years [1]–[4]. Single-phase VSIs can work either in grid-connected mode or stand-alone mode, and are closely combined with the pulsewidth modulation (PWM) technique and digital control technologies. In general, the most common application of single-phase VSIs in stand-alone mode lies in off-grid power generation systems and power equipment like uninterrupted power supply (UPS) [5], [6]. This kind of converter is normally designed with an *LC* smoothing filter and closed-loop control structure, to produce a stable sinusoidal output voltage of constant magnitude and frequency with fast dynamic response and zero steady-state error [7].

To regulate the output voltages of single-phase VSIs in stand-alone mode, various control techniques, including stability analysis and parameters design methods, have been proposed. Apart from the conventional single or dual closed-loop control strategy based on the proportional–integral–derivative (PID) regulators, the deadbeat control [8], [9], the repetitive control [10], [11], the sliding-mode control [12], [13], and the proportional–resonant (PR) control [14], [15] are most frequently used control methods. The deadbeat control possesses excellent dynamic performance and wide control bandwidth due to the direct regulation of the inverter output voltage, but it is highly sensitive to system parameters and cannot remove the steady-state errors of system. The repetitive control is mainly designed for systems with periodic output, and it is effective in suppressing the harmonics of the output voltage. However, poor rejection of aperiodic disturbance, slow dynamics, and low tracking accuracy normally limits the application of this control technique. The sliding-mode control exhibits superiority in the dynamic behaviors, and implementation simplicity, and less additional regulation. Despite these advantages, sliding-mode control also suffers from obvious flaw of dynamic tracking accuracy. PR control is well known for its capacity of effectively eliminating the steady-state error in tracking ac signals and applicability of instantaneous voltage control for single-phase VSIs, and the PR control scheme containing multiple resonant units is a prevalent

method for harmonic compensation. But PR control is also constrained by the disadvantages of poor dynamic response to input changes and great sensitivity to deviations of sampling signals. In addition to these methods, some intelligent control approaches, such as adaptive control [16], neural network control [17], and fuzzy control [18], have also been presented in literatures. Generally, intelligent control methods are applied in practical applications for their advantages of strong robustness, low dependence on system parameters, and adaptive characteristics, which means that these approaches are suitable for nonlinear, time-varying or delay systems. However, due to the high complexity, limited control precision, and the lack of complete analysis and design guidelines, intelligent control methods are still not mature for converter systems to a certain extent.

In [19]–[21], a synchronous reference frame (SRF) control scheme for the single-phase VSI is presented. This control technique has attracted increasing interests due to its advantage of realizing a zero steady-state error by employing the conventional PI regulators in the SRF. To utilize this control technique, a fictitious second phase voltage is generated by the orthogonal-signal-generation (OSG) techniques to emulate a two-phase system, and the electrical signals are transformed to the SRF for effective control. Stability analysis and parameters design of digital-controlled single-phase VSIs with SRF voltage control are illustrated in [22], [23], by using equivalent transfer functions in stationary frame to overcome the analytical difficulty caused by coordinate transformation. However, the switching converters are nonlinear systems in nature, whose nonlinear characteristics are originated from both the power circuits and the control systems. Despite the broad applicability for switching converters, linear analysis methods like transfer functions suffer from the drawbacks of poor description for the nonlinearity and the fast-scale dynamics of switching converters, and incomplete stability prediction. On the contrary, the nonlinear approaches are capable of illustrating the slow- and fast-scale stability of the switching converters directly, and well adapted to present the nonlinear phenomena such as bifurcation and chaos in switching converters. Furthermore, the nonlinear approaches have been shown to be suitable for analyzing the digital-controlled switching converters reliably and accurately [24], [25].

In retrospect, the nonlinear theory is first adopted to study the nonlinear phenomena in dc–dc converters [26]–[28] and then extended to the other switching converters like PWM inverters [29]–[34], power factor correction (PFC) circuits [35], [36]. Several nonlinear control strategies for switching converters have been developed, such as the Lyapunov function-based and passivity-based control methods [30]–[34]. These control strategies can not only reserve the nonlinearities of the switching converters, but also ensure high control performances, including global stability, improved waveforms, zero steady-state error, and fast dynamics under linear or nonlinear load conditions. For stability analysis of switching converters, the bifurcation diagram method, the Lyapunov exponent method, and the Jacobian matrix method are the three main nonlinear approaches [29]. These three methods are normally based on the discrete-time model, and for a certain system, they can be applied simultaneously. The bifurcation diagram method describes system stability through the bifurcation diagrams. To utilize this method, iterative calculation determined by the discrete-time model should be implemented to compute numerous values of state variables under different bifurcation parameters. By plotting the calculated state variable values with the corresponding bifurcation parameter values into graphs with certain rules, bifurcation diagrams can be produced. In an ordinary bifurcation diagram, a bifurcation parameter is on one axis as an independent variable and a state value on the other axis as a dependent variable. System is stable on the bifurcation parameter intervals where one certain bifurcation parameter value corresponds to only one state variable value. System goes into the unstable period-n state on the bifurcation parameter intervals where one certain value of bifurcation parameter corresponds to n ($n \geq 2$) state variable values. And on the bifurcation parameter intervals where one certain bifurcation parameter value corresponds to infinite state variable values, system operates in chaotic state which is highly unstable [28]. Bifurcation diagram presents the stable and unstable parameter intervals, and the processes of bifurcations in a straightforward manner. However, to use this method, state variables are required to be precisely calculated in iterations, which is not available for all discrete-time models, and may lead to a huge computational burden.

The Lyapunov exponent method depicts the system stability by employing the Lyapunov exponent. An n-dimensional system possesses n Lyapunov exponents, and system stability can be described by the maximum one. The stability criteria of the Lyapunov exponent method is as follows: negative maximum Lyapunov exponents indicate that the system is stable, zero maximum Lyapunov exponents indicate that system operates in critical steady state, and positive maximum Lyapunov exponents indicate that the system is chaotic. The maximum Lyapunov exponent can be calculated by several approaches [37]. By plotting the maximum Lyapunov exponent with the selected system parameter into graphs, the maximum Lyapunov exponent spectrums can be obtained. In the maximum Lyapunov exponent spectrum, the stable and unstable parameter intervals can be demonstrated clearly. The principle of the Jacobian matrix method is to determine system's stability on the basis of the eigenvalues of the Jacobian matrix at the fixed point of the discrete-time model [38]. The stability criteria of the Jacobian matrix method can be expressed as follows: when all eigenvalues of the Jacobian matrix at the fixed point of the discrete-time model are located in the unit circle on the complex plane, the system is stable, and when any eigenvalue lies outside the unit circle, the system becomes chaotic. For the critical situations that some eigenvalues lie on the unit circle but no eigenvalue lies outside it, the system moves into the critical steady state [39], [40]. The Jacobian matrix method is carried out in one single switching cycle, which is a sufficiently short time period that can be defined as the so-called "fast scale." It reveals the system dynamic behavior, which possesses low amplitude or high frequency close to the switching frequency, so the stability described by this feature is usually called the fast-scale stability of switching converters. On the

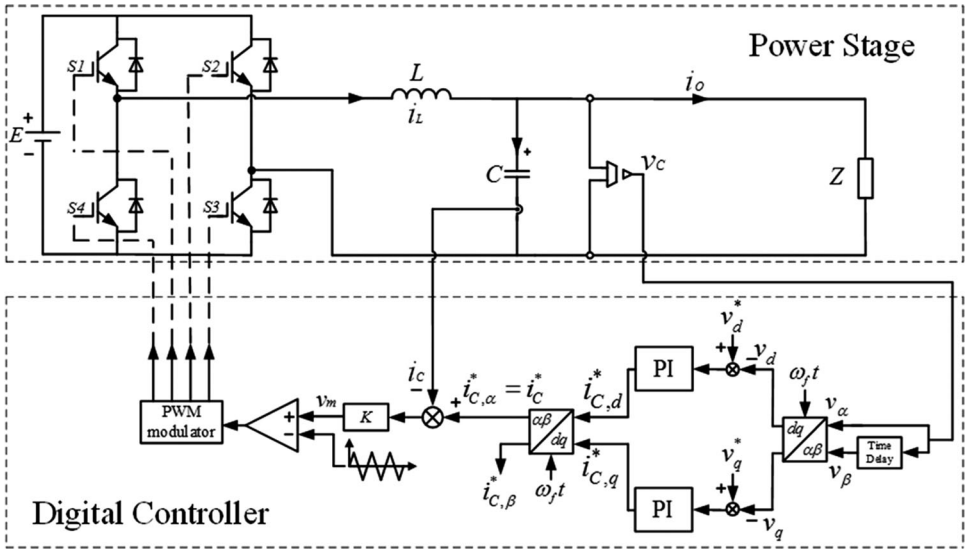

Fig. 1. System structure of the digital-controlled single-phase VSI with SRF voltage control in stand-alone mode.

contrary, the bifurcation diagram method and the Lyapunov exponent method are both implemented in multiple successive switching cycles, which constitute a much longer time period that can be defined as the "slow-scale," and they normally demonstrate the system dynamic property with a frequency that is much lower than the switching frequency, and the stability characteristics can be called the slow-scale stability of switching converters.

Without doubt, discrete-time model is significant for stability analysis of the switching converters using the bifurcation diagram method, the Lyapunov exponent method, or the Jacobian matrix method. Discrete-time models of switching converters are usually derived by using discrete maps. Depending on the mapping points, discrete maps mainly include a stroboscopic map, a synchronous switching map, an asynchronous switching, and a two-by-two map, while the stroboscopic map is the most popular one [41], [42]. In a stroboscopic map, the state variables at the end point are derived by solving the state equations with state variables at the starting point within one switching cycle, which is equivalent to sampling the state variables with switching frequency. For stability analysis, a stroboscopic model defined by the stroboscopic map is proved to be reliable and accurate. However, the inherent piecewise-linear property of switching converters can bring great difficulties in calculating the exact solutions of the state equations during a switching cycle, especially for state equations of high order, which creates a limitation for a stroboscopic map. For the sake of facilitating the modeling of converters with a stroboscopic map, the state-space averaging (SSA) technique has been proposed [24], [43]. In [24], a single-phase VSI with the capacitor voltage and the inductor current feedback control in stationary frame, as well as a current-controlled BOOST chopper, is investigated by the Jacobian matrix method. In addition, a comparison of stroboscopic models derived by using the state-space average technique and precisely solving the state equations is presented to confirm that the former is accurate enough for analyzing the nonlinear characteristics of switching converters with high switching frequency.

In this paper, the detailed stability analysis of a digital-controlled single-phase VSI with SRF voltage control is presented by employing nonlinear approaches. The stroboscopic model of the inverter is established by using the SSA technique and analyzed by the Jacobian matrix method and the Lyapunov exponent method under control parameters variations. The stability regions of the inverter are obtained, and the analysis results show that, for the studied stroboscopic model, the fast-scale stability described by the Jacobian matrix method is equivalent to the slow-scale stability determined by the Lyapunov exponent method. Experimental results under resistive load, inductive–resistive load, and diode rectifier load conditions are presented to validate the theoretical analyses.

This paper is organized as follows. Section II presents the modeling of the single-phase VSI with SRF voltage control, and the stroboscopic model is derived. Section III provides the stability analyses of the inverter under the parameter variations of voltage loop. The stability analysis of the inverter under the parameter variations of current loop is presented in Section IV. Section V presents the experimental results to validate the theoretical analyses. Section VI concludes the paper.

II. System Modeling of Single-Phase VSI With SRF Voltage Control

Fig. 1 illustrates the structure of the studied digital-controlled single-phase VSI with SRF voltage control, which works in the stand-alone mode with an *LC* filter and the load *Z*. As can be seen, the filter capacitor voltage plus the filter capacitor current feedback control strategy is applied in this inverter system. Specifically, to emulate a two-phase system, the filter capacitor voltage v_C is taken as the α-axis input v_α for the Park's transformation and a fictitious electrical signal generated by the time delay block serves as the β-axis input v_β. In the stationary

TABLE I
PARAMETERS OF THE PROTOTYPE INVERTER SYSTEM

Parameter	Symbol	Value
DC-link voltage	E	50 V
Filter inductance	L	2 mH
Filter capacitance	C	2.2 μF
Sampling frequency	f_s	20 kHz
Switching frequency	f	20 kHz
d-Axis reference value	v_d^*	40 V
Angular frequency	ω_f	100 π rad/s

frame, the reference of v_C is defined as $v_C^* = V_{Cm}\cos(\omega_f t)$, with a fundamental cycle of $T_f = 2\pi/\omega_f$, so the time delay block delays v_C for one-quarter of T_f in time domain to ensure that its output v_β is orthogonal to v_C. The d-axis reference voltage v_d^* in the SRF is then set to the desired magnitude V_{Cm}, and the q-axis reference voltage v_q^* is equal to zero. After the same PI control for the deviation of both v_d and v_q, the electrical signals are transformed back to stationary frame by inverse Park's transformation, and the α-axis output is subsequently taken as the reference for the filter capacitor current i_C in current loop, since only α-axis quantities correspond to the real system. In the current loop, the deviation of i_C is regulated by a proportional controller, and then modulation signal v_m is finally produced.

The main parameters of the studied PWM inverter with a reduced-scale power rating are listed in Table I except three important control parameters, proportional gain k_i and integral gain k_p of the PI controllers in voltage loop, and the proportional gain K in current loop, since their effect on the system stability is investigated in Sections III and IV.

A. System Modeling Under Resistive Load Condition

In this case, load Z in Fig. 1 is regarded as a linear resistor of 20 Ω, which is denoted by R. Since the PWM inverter in stand-alone mode is composed of power stage and digital controller, these two parts are modeled simultaneously in the following parts. The stroboscopic map used for the modeling is shown in Fig. 2.

For the power stage, the filter inductor current i_L and filter capacitor voltage v_C are considered as state variables. In one switching cycle, the state in which S1 and S3 are on, and S2 and S4 are off is defined as State 1, while the state in which S2 and S4 are on, and S1 and S3 are off is defined as State 2. State equation for State 1 is derived as

$$\dot{\mathbf{x}} = \mathbf{A_1}\mathbf{x} + E\mathbf{B_1}. \tag{1}$$

And the state equation for State 2 is written as

$$\dot{\mathbf{x}} = \mathbf{A_2}\mathbf{x} + E\mathbf{B_2} \tag{2}$$

where

$$\mathbf{x} = \begin{bmatrix} i_L & v_C \end{bmatrix}^T, \quad \mathbf{A_1} = \mathbf{A_2} = \mathbf{A} = \begin{bmatrix} 0 & -\frac{1}{L} \\ \frac{1}{C} & -\frac{1}{RC} \end{bmatrix},$$

$$\mathbf{B_1} = \begin{bmatrix} \frac{1}{L} \\ 0 \end{bmatrix}, \quad \mathbf{B_2} = \begin{bmatrix} -\frac{1}{L} \\ 0 \end{bmatrix}.$$

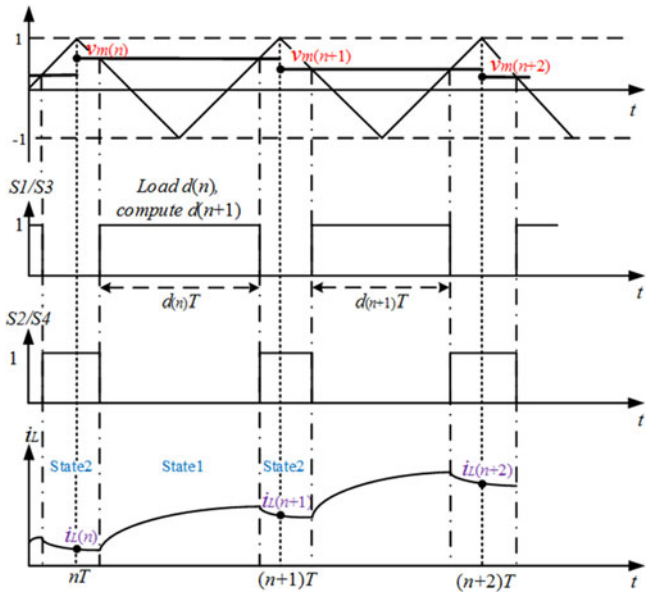

Fig. 2. Stroboscopic map of the single-phase PWM inverter.

The duty ratio, denoted as d, is defined as the duration of State 1 in one switching cycle.

In Fig. 2, it can be seen that the PWM inverter switches between State 1 and State 2 in a switching cycle, which makes the complete state equation piecewise linear and complicates the modeling process. To overcome this problem, the SSA technique is employed. By averaging the durations of State 1 and State 2 in one switching cycle, a simplified state equation is derived to replace the original one, which is written as

$$\dot{\mathbf{x}} = d(\mathbf{A_1}\mathbf{x} + E\mathbf{B_1}) + (1-d)(\mathbf{A_2}\mathbf{x} + E\mathbf{B_2}) \tag{3}$$

namely

$$\dot{\mathbf{x}} = \mathbf{A}\mathbf{x} + E\mathbf{B} \tag{4}$$

where

$$\mathbf{B} = \begin{bmatrix} \frac{2d-1}{L} \\ 0 \end{bmatrix}.$$

As illustrated in Fig. 2, taking the filter inductor current value $i_L(n) = i_L(nT)$ and filter capacitor voltage value $v_C(n) = v_C(nT)$ at the beginning of nth switching cycle for initial conditions to solve (4), the filter inductor current value $i_L(n+1) = i_L[(n+1)T]$ and filter capacitor voltage value $v_C(n+1) = v_C[(n+1)T]$ at the beginning of $(n+1)$th switching cycle are derived as

$$\begin{cases} i_L(n+1) = i_L[(n+1)T] = e^{\alpha T}(K_1\cos\beta T + K_2\sin\beta T) \\ \qquad -\frac{1}{R}[1-2d(n)]E \\ v_C(n+1) = v_C[(n+1)T] = e^{\alpha T}(K_3\cos\beta T + K_4\sin\beta T) \\ \qquad -[1-2d(n)]E \end{cases} \tag{5}$$

where $d(n)$ is the duty ratio in the nth switching cycle, and the expressions of α, β, K_1, K_2, K_3, and K_4 are found in Appendix A.

For the digital controller, the duty ratio d is regarded as the state variable. In terms of the discrete map in Fig. 2, one switching cycle delay for the digital control is taken into account, and thus, the stroboscopic model of control stage are expressed as

$$d(n+1) = \frac{1}{2}v_m(n) + \frac{1}{2} \tag{6}$$

where

$$\begin{aligned} v_m(n) &= K[i_C^*(n) - i_C(n)] \\ i_C^*(n) &= k_p v_d^*(\cos\omega_f nT) - k_p v_C(nT) + nk_i v_d^* T(\cos\omega_f nT) \\ &\quad - k_i T(\cos\omega_f nT)\sum_{k=1}^{n}[v_C(kT)\cos(\omega_f kT) \\ &\quad + v_C(kT-\tau)\sin(\omega_f kT)] - k_i T(\sin\omega_f nT) \\ &\quad \times \sum_{k=1}^{n}[v_C(kT)\sin(\omega k_f T) - v_C(kT-\tau)\cos(\omega_f kT)] \\ \tau &= \frac{\pi}{2\omega_f}, \quad i_C(n) = i_L(n) - \frac{1}{R}v_C(n). \end{aligned}$$

And $d(n+1)$ is the duty ratio in the $(n+1)$th switching cycle. $v_m(n) = v_m(nT)$, $i_C^*(n) = i_C^*(nT)$, and $i_C(n) = i_C(nT)$ represent the modulation signal, the reference filter capacitor current, and the filter capacitor current in the nth switching cycle, respectively. Thus, the complete stroboscopic model of the PWM inverter is described by (5) and (6). Apparently, this model is linear in one switching cycle, but on a longer time interval, it is still a nonlinear description for the PWM inverter, which can be used to investigate the dynamic properties of the system, and the accuracy of this approach will be verified by experimental results.

B. System Modeling Under Inductive–Resistive Load Condition

In this case, the load Z shown in Fig. 1 is composed of a linear resistor of 10 Ω and a linear inductor of 4 mH, which are denoted as R_1 and L_1, respectively. Besides filter inductor current i_L and filter capacitor voltage v_C, output current i_o is also taken as a state variable for system modeling. By using the SSA technique, the state equation of power stage is derived as

$$\dot{\mathbf{x}} = \mathbf{A_3}\mathbf{x} + E\mathbf{B_3} \tag{7}$$

where

$$\mathbf{x} = \begin{bmatrix} i_L & v_C & i_o \end{bmatrix}^T, \quad \mathbf{A_3} = \begin{bmatrix} 0 & -\frac{1}{L} & 0 \\ \frac{1}{C} & 0 & -\frac{1}{C} \\ 0 & \frac{1}{L_1} & -\frac{R_1}{L_1} \end{bmatrix},$$

$$\mathbf{B_3} = \begin{bmatrix} \frac{2d-1}{L} \\ 0 \\ 0 \end{bmatrix}.$$

Taking the filter inductor current value $i_L(n) = i_L(nT)$, the filter capacitor voltage value $v_C(n) = v_C(nT)$, and the output current value $i_o(n) = i_o(nT)$ at the beginning of nth switching cycle for initial conditions to solve (7), the filter inductor current value $i_L(n+1) = i_L[(n+1)T]$, the filter capacitor voltage value $v_C(n+1) = v_C[(n+1)T]$, and the output current value $i_o(n+1) = i_o[(n+1)T]$ at the beginning of $(n+1)$th switching cycle are obtained as (8), shown at the bottom of the page, where the coefficients r, α_1, β_1, K_5, K_6, and K_7 are defined in Appendix B.

And the modeling of the digital controller is the same as the case under the resistive load condition

C. System Modeling Under Diode Rectifier Load Condition

In this case, the structure of the studied PWM inverter is shown in Fig. 3. To eliminate the odd harmonics component in the output voltage, the harmonic suppression scheme which consists of a series of PI controllers in the SRFs with harmonic angular frequency, is adopted. The load resistor and the capacitor of the diode bridge rectifier, denoted as R_o and C_o, are 50 Ω and 2 mF, respectively. An additional inductor of 2 mH is employed to form an *LC* filter with C_o, which is denoted as L_a.

Due to the operational characteristic of diode-bridge rectifier, the on-off states of the four diodes in the rectifier are indeterminate for State 1 and State 2 during any switching cycle, which results in great difficulty in determining the output current i_o of the PWM inverter. In fact, accurate time-domain i_o, namely, the input current of the diode bridge rectifier needed for system modeling, can be obtained only under a certain input voltage of the diode-bridge rectifier, which possesses an explicit expression on a time interval composed of one or several successive fundamental periods, rather than a switching cycle [44]. Furthermore, the conduction angles of diode bridge rectifier are normally calculated by the iterative algorithms like Newton–Raphson method or Gauss–Seidel approach, which is complex and time consuming [45]. Therefore, precise modeling of the PWM inverter under diode rectifier load condition is nearly impossible with the stroboscopic map. However, by

$$\begin{cases} i_L(n+1) = i_L[(n+1)T] = K_5 e^{rT} + e^{\alpha_1 T}(K_6\cos\beta_1 T + K_7\sin\beta_1 T) \\ v_C(n+1) = v_C[(n+1)T] = -rK_5 L e^{rT} - Le^{\alpha_1 T}(\alpha_1 K_6 + \beta_1 K_7)\cos\beta_1 T - Le^{\alpha_1 T}(\alpha_1 K_7 - \beta_1 K_6)\sin\beta_1 T + [2d(n)-1]E \\ i_o(n+1) = i_o[(n+1)T] = (LCK_5 r^2 + K_5)e^{rT} + e^{\alpha_1 T}(K_6\cos\beta_1 T + K_7\sin\beta_1 T) + LC(\alpha_1 K_6 + \beta_1 K_7) \\ \qquad \times e^{\alpha_1 T}(\alpha_1\cos\beta_1 T - \beta_1\sin\beta_1 T) + LC(\alpha_1 K_7 - \beta_1 K_6)e^{\alpha_1 T}(\alpha_1\sin\beta_1 T + \beta_1\cos\beta_1 T) \end{cases} \tag{8}$$

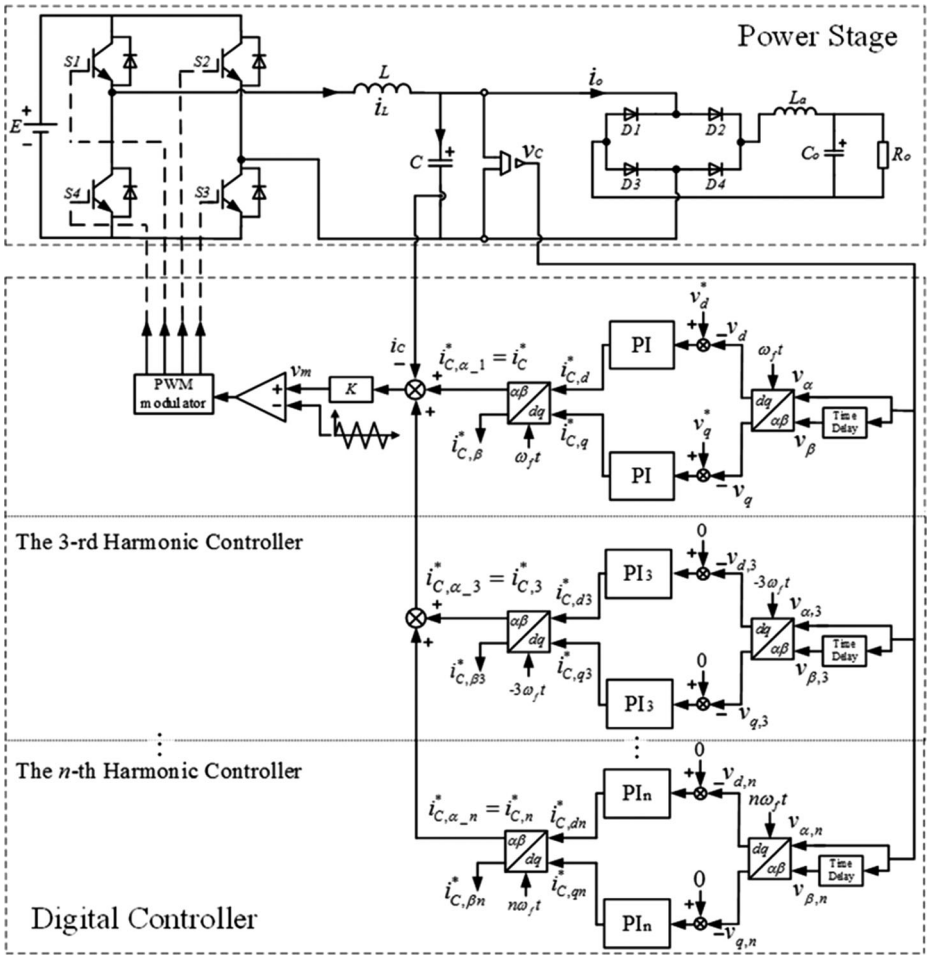

Fig. 3. Structure of the digital-controlled single-phase VSI with diode rectifier load.

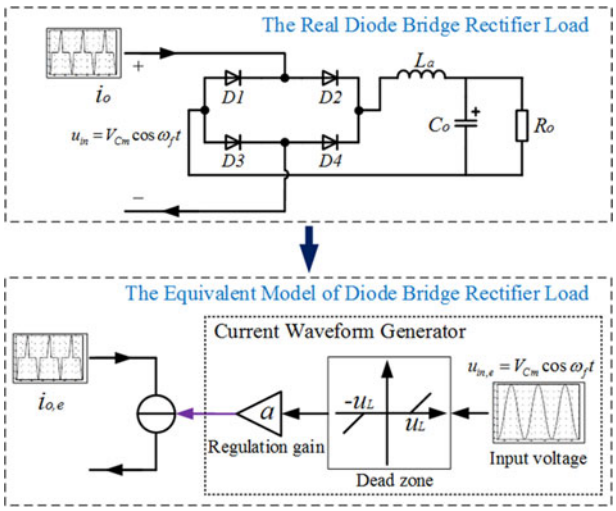

Fig. 4. Equivalent model of the diode bridge rectifier load.

using an equivalent controlled current source (CCS) to represent the diode rectifier load, the approximate system modeling can be conducted. A simple and practical equivalent model of the diode rectifier load is proposed in [46] and described in Fig. 4.

Clearly, this model is an equivalent current source controlled by a dead-zone block with a proportional regulator and sinusoidal input voltage. Since the input voltage of the real diode rectifier $u_{\rm in}$ is quite close to the desired sinusoidal voltage $v_C^* = V_{Cm}\ \cos(\omega_f t)$ under the steady state of the inverter, then supposing the input voltage of the equivalent model $u_{{\rm in},e}$ is also $v_C^* = V_{Cm}\ \cos(\omega_f t)$, and thus, the parameters of the equivalent model, including the regulation gain a, the dead-zone limit u_L can be selected to achieve the best possible approximation of the real diode rectifier input current by simulation. Finally, the time-domain explicit expression of the PWM inverter output current i_o is approximately written as

$$i_o(t) \approx i_{o,e}(t) = \begin{cases} a[(V_{Cm}\ \cos\omega_f t) - u_L], & V_{Cm}\ \cos\omega_f t > u_L \\ 0, & -u_L \le V_{Cm}\ \cos\omega_f t \le u_L \\ a[-u_L - (V_{Cm}\ \cos\omega_f t)], & V_{Cm}\ \cos\omega_f t < -u_L \end{cases}. \tag{9}$$

Once again, by taking the filter inductor current i_L and the filter capacitor voltage v_C as the state variables, the simplified state equation of power stage is derived as

$$\dot{\mathbf{x}} = \mathbf{A_4}\mathbf{x} + \mathbf{B_4} \tag{10}$$

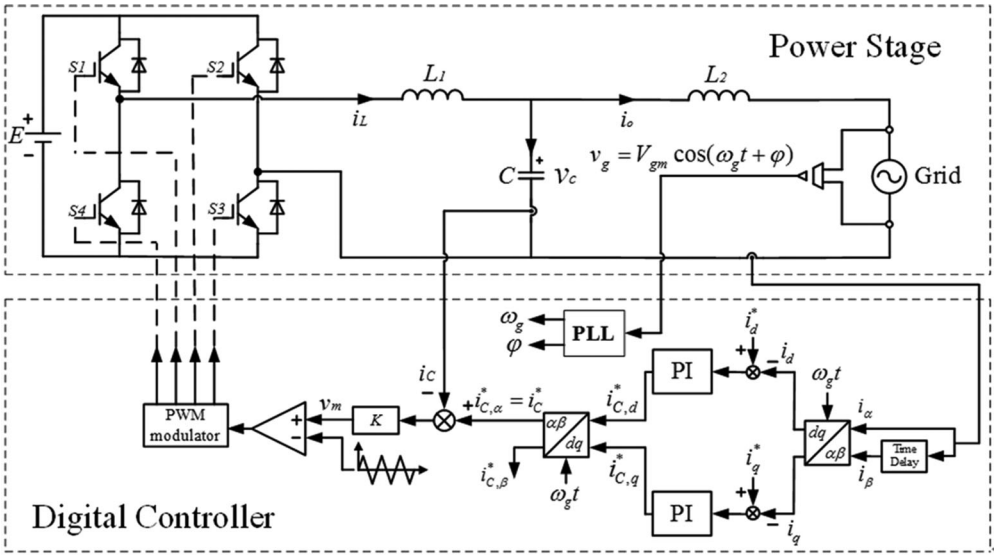

Fig. 5. System structure of the digital-controlled single-phase VSI with SRF control loop in grid-connected mode.

where

$$\mathbf{x} = \begin{bmatrix} i_L & v_C \end{bmatrix}^T, \quad \mathbf{A_4} = \begin{bmatrix} 0 & -\frac{1}{L} \\ \frac{1}{C} & 0 \end{bmatrix}, \quad \mathbf{B_4} = \begin{bmatrix} \frac{(2d-1)E}{L} \\ -\frac{1}{C} io \end{bmatrix}.$$

Mathematically, taking the filter inductor current value $i_L(n) = i_L(nT)$ and the filter capacitor voltage value $v_C(n) = v_C(nT)$ at the beginning of the *n*th switching cycle for the initial conditions to solve (10), the filter inductor current value $i_L(n+1) = i_L[(n+1)T]$ and the filter capacitor voltage value $v_C(n+1) = v_C[(n+1)T]$ can be derived.

For the digital controller, $v_m(n)$ is modified as

$$v_m(n) = \left[K \sum_{m=0}^{n} i^*_{C,\alpha\_2m+1}(n) \right] - K i_C(n). \qquad (11)$$

The output of the (2 m + 1)th order harmonic controller is represented as (12), presented at the bottom of the page, where $\tau = \pi/2\omega_f$, $i_C(n) = i_L(n) - i_o(n)$.

The parameters $k_{p,2m+1}$ and $k_{i,2m+1}$ are the proportional gain and integral gain of the (2m + 1)th harmonic controller, $d(n+1)$ keeps the same form as the case under resistive load condition.

D. Discussion on the System Modeling of the PWM Inverter in the Grid-Connected Mode

In the grid-connected mode, an *LCL* filter is employed to replace the *LC* filter used in stand-alone mode, as presented in Fig. 5. The inverter output current i_o must be controlled to gain the same frequency as the grid voltage, which is also mainly implemented in the SRF. Supposing the grid voltage is $v_g = V_{gm}\cos(\omega_g t + \varphi)$, the reference of i_o is accordingly defined as $i_o^* = I_{om}\cos(\omega_g t + \varphi)$. As a result, the *d*-axis reference current i_d^* is determined as $I_{om}\cos\varphi$, and the *q*-axis reference current i_q^* is set as $I_{om}\sin\varphi$. The angular frequency ω_g and phase φ of the grid voltage are identified by a single-phase phase-locked loop (PLL), and normally, ω_g and φ are constant for a definite single-phase grid. Taking filter inductor current i_L, output current i_o, filter capacitor v_C as state variables, and following the aforementioned modelling steps, the stroboscopic model of the

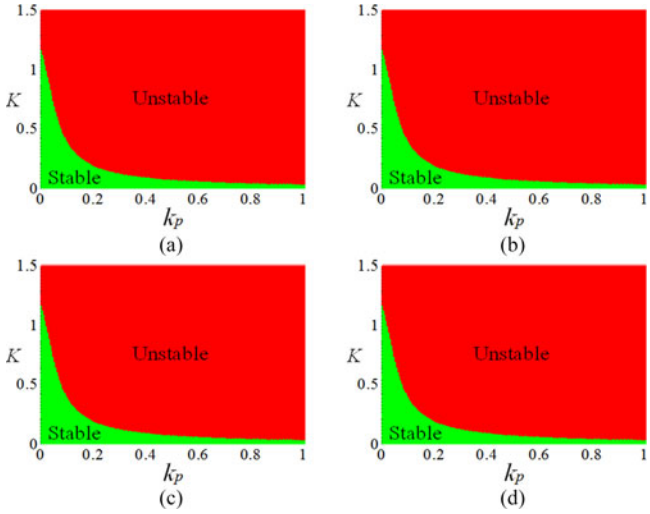

Fig. 6. Stability regions of the single-phase VSI with SRF voltage control under different k_i. (a) $k_i = 20$; (b) $k_i = 40$; (c) $k_i = 60$; (d) $k_i = 80$.

$$i^*_{C,\alpha\_2m+1}(n) = -k_{p,2m+1}v_C(nT) - k_{i,2m+1}T\cos[(2m+1)\omega_f nT]\sum_{k=1}^{n}\{v_C(kT)\cos[(2m+1)\omega_f kT] + v_C(kT-\tau)$$
$$\times \sin[(2m+1)\omega_f kT]\} - k_{i,2m+1}T\sin[(2m+1)\omega_f nT]\sum_{k=1}^{n}\{v_C(kT)\sin[(2m+1)\omega_f kT] - v_C(kT-\tau)\cos[(2m+1)\omega_f kT)]\} \qquad (12)$$

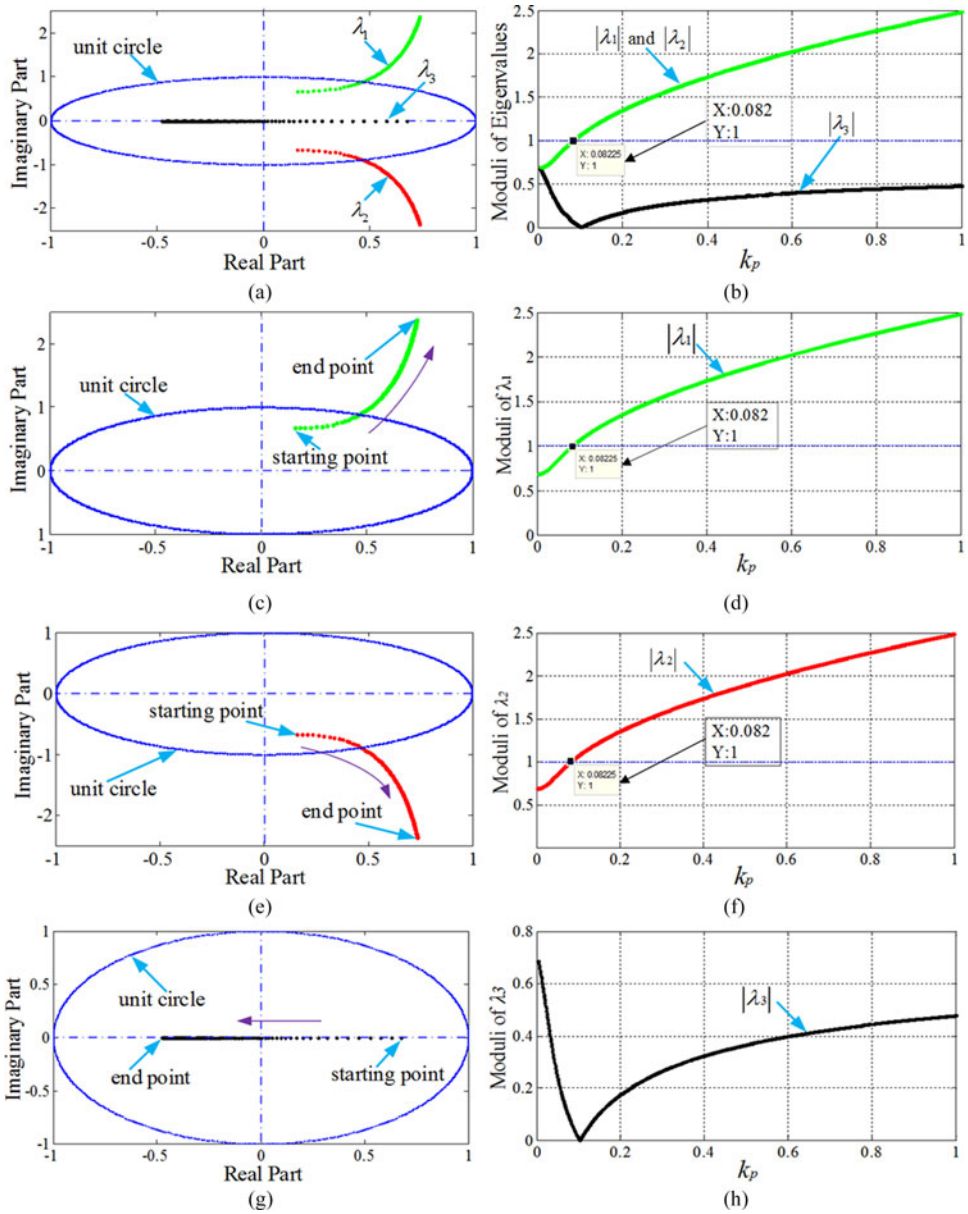

Fig. 7. Loci and moduli of three eigenvalues of the Jacobian matrix when k_p varies under condition of $k_i = 20$ and $K = 0.5$. (a) Loci of $\lambda_1, \lambda_2, \lambda_3$. (b) Moduli of $\lambda_1, \lambda_2, \lambda_3$. (c) Locus of λ_1. (d) Modulus of λ_1. (e) Locus of λ_2. (f) Modulus of λ_2. (g) Locus of λ_3. (h) Modulus of λ_3.

PWM inverter in grid-connected mode can be established, and this model can also be analyzed by the methods demonstrated in Sections III and IV.

III. Stability Analysis Under Variations of Control Parameters in Voltage Loop

Because the fictitious second phase voltage v_β is generated by delaying v_C for one-quarter of fundamental cycle of v_C^*, it is extremely difficult to obtain the exact values of v_β at the beginning of any switching cycle for the direct iteration defined by the stroboscopic model. Thus, the Jacobian matrix method and the Lyapunov exponent method are employed for the stability analysis of the PWM inverter.

A. Stability Analysis Under Resistive Load by Using the Jacobian Matrix Method

Denoting the fixed point of the stroboscopic model as $(i_L^*,\ v_C^*, d^*)$ and substituting it into (5) and (6), and supposing $i_L(n+1) = i_L(n) = i_L^*,\ v_C(n+1) = v_C(n) = v_C^*$, $d(n+1) = d(n) = d^*$, the Jacobian matrix at the fixed point is derived as (13), where the matrix elements are listed in Appendix C.

$$\mathbf{J} = \left[\begin{array}{ccc} \frac{\partial i_L(n+1)}{\partial i_L(n)} & \frac{\partial i_L(n+1)}{\partial v_C(n)} & \frac{\partial i_L(n+1)}{\partial d(n)} \\ \frac{\partial v_C(n+1)}{\partial i_L(n)} & \frac{\partial v_C(n+1)}{\partial v_C(n)} & \frac{\partial v_C(n+1)}{\partial d(n)} \\ \frac{\partial d(n+1)}{\partial i_L(n)} & \frac{\partial d(n+1)}{\partial v_C(n)} & \frac{\partial d(n+1)}{\partial d(n)} \end{array}\right]\Bigg|_{\left(i_L^*, v_C^*, d^*\right)}. \tag{13}$$

As can be seen, the Jacobian matrix in (13) is independent to any fixed point of the stroboscopic model, and this is because the stabilities of different fixed points are regarded as consistent for the established SSA model.

To investigate the fast-scale stability of the PWM inverter with a low computation cost, four typical values of k_i, including 20, 40, 60, 80, are taken into account to find the stability regions by the Jacobian matrix method, which are depicted in Fig. 6. In Fig. 6, the green zones represent the control parameters that enable all eigenvalues of the Jacobian matrix in (13) to be located in the unit circle on the complex plane, which means that the PWM inverter is stable. While the red zones represent parameters that make at least one eigenvalue of the Jacobian matrix lies on or outside the unit circle, which indicates that the PWM inverter is unstable.

It is obvious that, for a certain k_i, stable intervals of *K* become smaller as k_p increased. Conversely, when *K* increases, stable intervals of k_p decrease. However, the effect of parameter k_i on the stability of the PWM inverter is not distinct. This is because the Jacobian matrix in (13) contains only one component of k_i, which is $(1/2)KTk_i$. Owing to a sufficiently small switching cycle *T*, it is hard for $(1/2)KTk_i$ to exert a significant influence on the eigenvalues of the Jacobian matrix.

In consideration of the stability regions in Fig. 6 and without loss of generality, $k_i = 20$ and $K = 0.5$ is taken as a typical condition to analyze the effect of k_p on the fast-scale stability of the PWM inverter in detail. Denoting three eigenvalues of the Jacobian matrix in (13) as λ_1, λ_2, λ_3, and then their loci and moduli are illustrated in Fig. 7.

As shown in Fig. 7, λ_1 and λ_2 form a pair of complex conjugates, and λ_3 remains real on the studied interval consistently. When $0 < k_p < 0.082$, λ_1, λ_2, and λ_3 all lie in the unit circle, which suggests that the PWM inverter is stable. When $0.082 < k_p < 1$, λ_1 and λ_2 move outside the unit circle, while λ_3 still locates in it, which indicates that the PWM inverter becomes unstable. Thus, $k_p = 0.082$ is the critical point determining the stable and unstable state of the PWM inverter when $k_i = 20$ and $K = 0.5$.

B. Stability Analysis Under Resistive Load Condition by Using the Lyapunov Exponent Method

To validate the earlier results obtained by the Jacobian matrix method, the maximum Lyapunov exponents of the inverter are calculated to show its slow-scale stability. According to [37], the maximum Lyapunov exponent of a three-dimensional discrete system can be defined as

$$\lambda L = \max\left(\lambda_{L1}, \lambda_{L2}, \lambda_{L3}\right) \tag{14}$$

$$\begin{bmatrix}\lambda_{L1}\\ \lambda_{L2}\\ \lambda_{L3}\end{bmatrix} = \lim_{n\to\infty}\frac{1}{n}\ln\left|\left[\mathrm{eig}\left(JnJn-1\cdots J1\right)\right]\right| \tag{15}$$

where $eig(J_n\, J_{n-1} \ldots J_1)$ is the eigenvalue function of $J_n J_{n-1} \ldots J_1$ and J_n is the Jacobian matrix at the mapping point in the *n*th switching cycle. Moreover, in terms of the stroboscopic model in (5) to (6), it is possible to derive $J_1 = J_2 = \ldots = J_{n-1} = J_n = J$, in which *J* is the Jacobian matrix presented in (13).

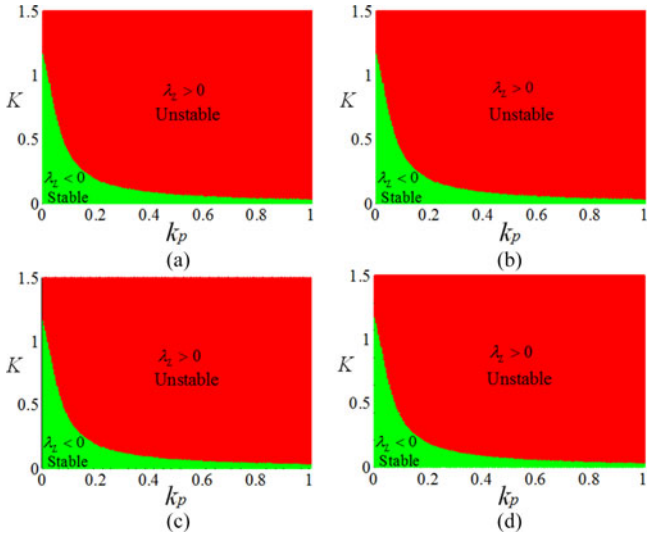

Fig. 8. Projections on the $K - k_p$ plane of maximum Lyapunov exponent spectrums under different k_i. (a) $k_i = 20$; (b) $k_i = 40$; (c) $k_i = 60$; (d) $k_i = 80$.

Fig. 8 illustrates the projections of maximum Lyapunov exponent spectrums on $K - k_p$ plane, under $k_i = 20, 40, 60, 80$. The red regions represent the control parameters leading to positive or zero maximum Lyapunov exponent, which are defined as unstable regions for the inverter. And the green regions match the control parameters producing negative maximum Lyapunov exponent, which are accordingly defined as stable regions. Clearly, Fig. 8 is almost the same as Fig. 6, and that means the slow-scale analysis results obtained by the Lyapunov exponent method are consistent with the fast-scale analysis results obtained by the Jacobian matrix method.

In fact, since $J_1 = J_2 = \ldots = J_{n-1} = J_n = J$, it is possible to obtain $\mathrm{eig}(J_n J_{n-1} \ldots J_1) = [\mathrm{eig}(J)]^n$ according to matrix theory, which yields

$$\begin{aligned}\begin{bmatrix}\lambda_{L1}\\ \lambda_{L2}\\ \lambda_{L3}\end{bmatrix} &= \lim_{n\to\infty}\frac{1}{n}\ln\left|\left[\mathrm{eig}\left(JnJn-1\cdots J1\right)\right]\right|\\ &= \lim_{n\to\infty}\frac{1}{n}\ln\left|\left[\mathrm{eig}\left(J\right)\right]^n\right|\\ &= \ln\left|\left[\mathrm{eig}\left(J\right)\right]\right|.\end{aligned} \tag{16}$$

Obviously, (16) shows a direct proof for the equivalence of the Jacobian matrix method and the Lyapunov exponent method, which also reveals that, in the sense of state space averaging, the fast-scale stability and slow-scale stability are almost the same for the studied PWM inverter model.

The maximum Lyapunov exponent spectrum on k_p is presented in Fig. 9 under condition of $k_i = 20$ and $K = 0.5$. As can be seen, when $k_p < 0.082$, the maximum Lyapunov exponent is negative, but when $k_p > 0.082$, the maximum Lyapunov exponent becomes positive, which means that $k_p = 0.082$ is the

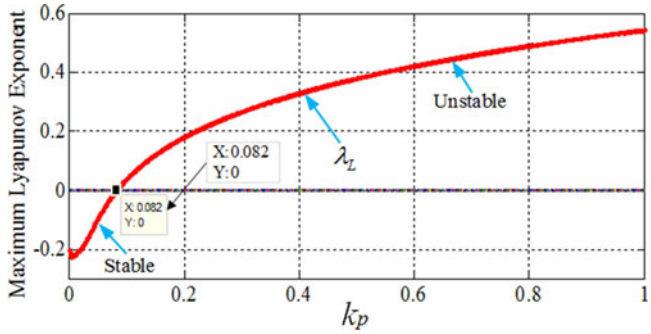

Fig. 9. Maximum Lyapunov exponent spectrum on k_p, under resistive load condition when $k_i = 20$ and $K = 0.5$.

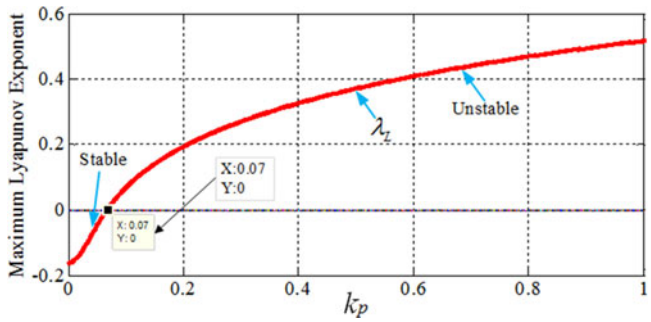

Fig. 10. Maximum Lyapunov exponent spectrum on k_p under inductive–resistive load condition when $k_i = 20$ and $K = 0.5$.

critical point when $k_i = 20$ and $K = 0.5$. Fig. 9 clearly shows a good consistency with Fig. 7.

C. Stability Analysis Under Inductive–Resistive Load Condition

In view of the consistency of the Jacobian matrix method and the Lyapunov exponent method proved in the analyses under resistive load condition, and the significant similarities between the system models of resistive and inductive–resistive load, it is reasonable to infer that the Jacobian matrix method and the Lyapunov exponent method are also coincident for inductive–resistive load, which reveals the fact that inductive–resistive load is inherently a kind of linear load. Therefore, for the sake of brevity, only the Lyapunov exponent method is adopted to investigate the effect of k_p on the stability of the PWM inverter when $k_i = 20$ and $K = 0.5$ in this part. The result is presented in Fig. 10. It is clear that, when $k_p < 0.07$, the maximum Lyapunov exponent is negative, but when $k_p > 0.07$, the maximum Lyapunov exponent becomes positive. So $k_p = 0.07$ is the critical point for system stability when $k_i = 20$ and $K = 0.5$ under the inductive–resistive load condition.

D. Stability Analysis Under Nonlinear Load Condition

Since the equivalent controlled current source is an approximated time-domain model of the diode rectifier with limited precision, so it is not very suitable for fast-scale stability analysis of the PWM inverter, which is sensitive to the model accuracy. Hence, in this part, only slow-scale stability analysis under diode rectifier load condition is conducted when $k_i = 20$ and

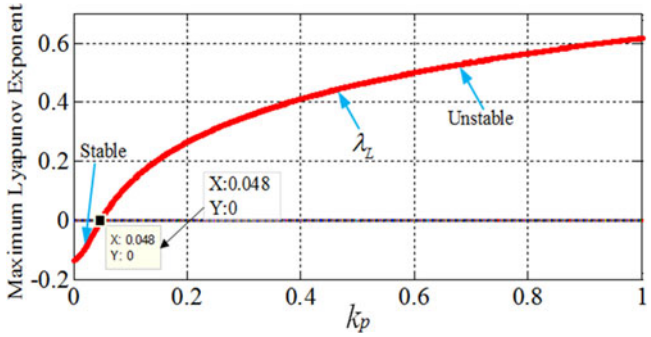

Fig. 11. Maximum Lyapunov exponent spectrum on k_p under nonlinear load condition when $k_i = 20$ and $K = 0.5$.

$K = 0.5$ by employing the equivalent diode rectifier model and the Lyapunov exponent method. The 3rd, 5th, 7th, 9th, and 11th harmonic control schemes are also added into the controller, and the parameters of them are selected by simulation method and considered as constants in the analysis. The result is presented in Fig. 11. It can be seen that, when $k_p < 0.048$, the maximum Lyapunov exponent is negative, but when $k_p > 0.048$, the maximum Lyapunov exponent becomes positive, which means that $k_p = 0.048$ is the critical point when $k_i = 20$ and $K = 0.5$ under nonlinear load condition. Apparently, the critical point of k_p is smaller under nonlinear load condition, compared to the cases of linear load conditions with same k_i and K.

IV. Stability Analysis Under Variations of Control Parameters in Current Loop

A. Stability Analysis Under Resistive Load Condition by Using the Jacobian Matrix Method

Considering the analysis in Section III, the effect of K on the stability of the PWM inverter is investigated under condition of $k_i = 20$ and $k_p = 0.04$ by the Jacobian matrix method first. Fig. 12 shows the loci and moduli of the three eigenvalues of the Jacobian matrix in (13), under variations of parameter K.

As shown in Fig. 12, on the studied interval of K, λ_1 and λ_2 are a pair of complex-conjugates. λ_3 is real and remains in the unit circle when K varies. When $K < 0.742$, λ_1 and λ_2 are located in the unit circle, but when $K > 0.742$, they move outside the unit circle. Hence the PWM inverter is stable when $K < 0.742$, but unstable when $K > 0.742$, and $K = 0.742$ is the critical point for the stability of the inverter when $k_i = 20$ and $k_p = 0.04$.

B. Stability Analysis Under Resistive Load Condition by Using the Lyapunov Exponent Method

Fig. 13 depicts the maximum Lyapunov exponent spectrum on K when $k_i = 20$ and $k_p = 0.04$ to validate the results in Fig. 12. In Fig. 13, it is shown that when $K < 0.742$, the maximum Lyapunov exponent is negative. However, when $K > 0.742$, the maximum Lyapunov exponent becomes positive, which means that $K = 0.742$ is the critical point. Obviously, Fig. 13 shows a good consistency with Fig. 12.

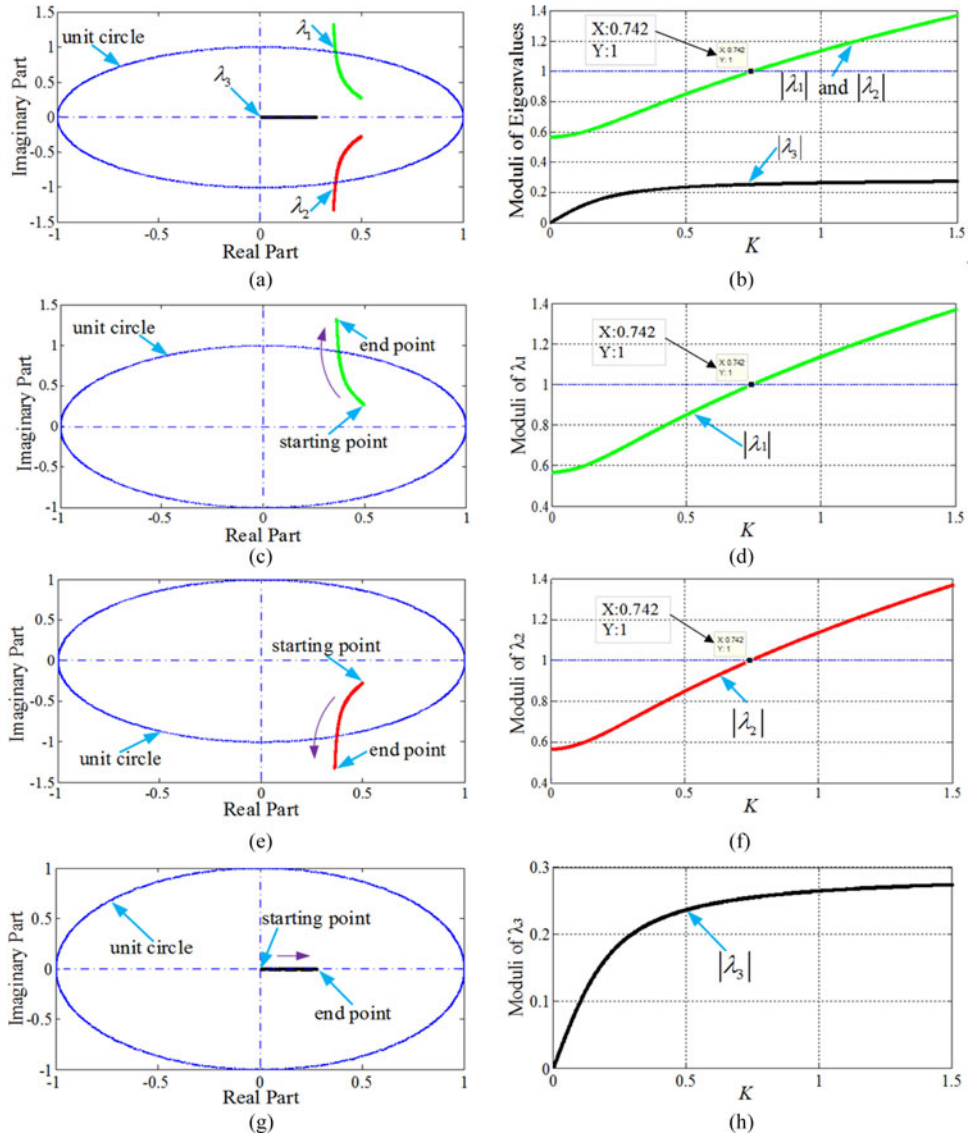

Fig. 12. Loci and moduli of the three eigenvalues of the Jacobian matrix when K varies under condition of $k_i = 20$ and $k_p = 0.04$. (a) Loci of λ_1, λ_2, λ_3. (b) Moduli of λ_1, λ_2, λ_3. (c) Locus of λ_1. (d) Modulus of λ_1. (e) Locus of λ_2. (f) Modulus of λ_2. (g) Locus of λ_3. (h) Modulus of λ_3.

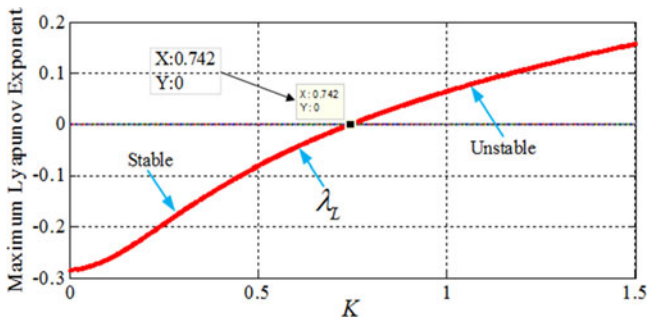

Fig. 13. Maximum Lyapunov exponent spectrum on K under resistive load condition when $k_i = 20$ and $k_p = 0.04$.

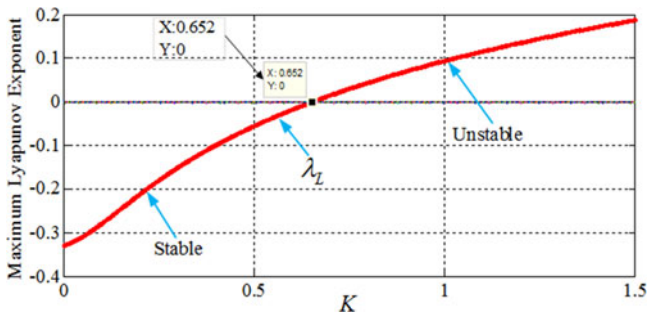

Fig. 14. Maximum Lyapunov exponent spectrum on K under inductive–resistive load condition when $k_i = 20$ and $k_p = 0.04$.

C. Stability Analysis Under Inductive–Resistive Load Condition

Under inductive–resistive load condition, the Lyapunov exponent method is adopted to investigate the effect of K on the stability of the PWM inverter when $k_i = 20$ and $k_p = 0.04$, and the result is shown as Fig. 14. It can be seen from Fig. 14, when $K < 0.652$, the maximum Lyapunov exponent is negative, but when $K > 0.652$, the maximum Lyapunov exponent becomes

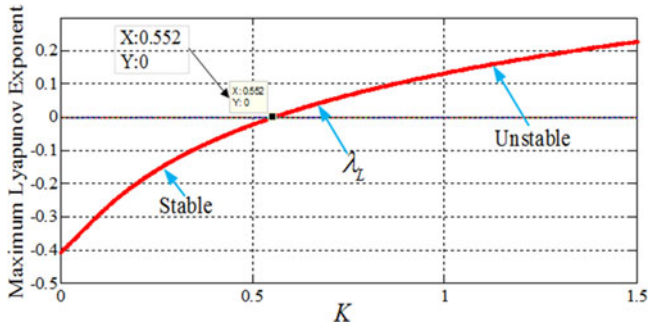

Fig. 15. Maximum Lyapunov exponent spectrum on *K* under nonlinear load condition when $k_i = 20$ and $k_p = 0.04$.

positive. So $K = 0.652$ is the critical point when $k_i = 20$ and $k_p = 0.04$ under inductive–resistive load condition.

D. Stability Analysis Under Nonlinear Load Condition

Under nonlinear load condition, slow-scale analysis is done to investigate the effect of *K* on the stability of the PWM inverter when $k_i = 20$ and $k_p = 0.04$, based on the equivalent model of diode rectifier and the Lyapunov exponent method. The 3rd, 5th, 7th, 9th, and 11th harmonic controllers are also employed in this case, and the parameters of them keep the same as those in the analysis on k_p in Section III-D. The analysis result is shown in Fig. 15. It is clear that, when $K < 0.552$, the maximum Lyapunov exponent is negative. However, when $K > 0.552$, the maximum Lyapunov exponent becomes positive, and that means $K = 0.552$ is the critical point under nonlinear load when $k_i = 20$ and $k_p = 0.04$. Evidently, this critical point of *K* is obviously much smaller than those of linear load conditions with same k_i and k_p.

V. Experimental Results and Discussions

According to the system structure in Fig. 1 and parameters in Table I, an experimental PWM inverter is built with a controller of TMS320F28335 DSP to verify the theoretical analyses. Voltage sensor HPT205A and current sensor ACS712ELCTR-05B-T are employed. The transformation ratio of HPT205A is 2:2, and its precision is 0.1%. The optimized range of ACS712ELCTR-05B-T is ±5 A, and its sensitivity is 185 mV/A. The dc-link voltage of the inverter is provided by a programmable dc power supply. The RIGOL digital oscilloscope is employed to record the time-domain waveforms and FFT results. The experimental results are presented as follows.

A. Experimental Results Under Resistive Load Condition

Fig. 16 shows the steady-state waveforms under resistive load condition for different k_p when $k_i = 20$, $K = 0.5$. It is evident that, waveforms of the filter capacitor voltage v_C and output current i_o are periodic and sinusoidal without any distortion when $k_p = 0.042$, which indicates that the PWM inverter is stable. When $k_p = 0.062$, waveforms of v_C and i_o become slightly distorted, which means that the PWM inverter is nearly critical stable. When k_p increases to 0.082, waveforms of v_C and i_o are obviously distorted, which suggests that the PWM inverter is oscillating.

And when $k_p = 0.102$, serious oscillation appears in the waveforms of v_C and i_o, and the PWM inverter is totally unstable. Therefore, experimental results in Fig. 16 are in accordance with the theoretical results that the PWM inverter becomes unstable when $k_p > 0.082$ for $k_i = 20$ and $K = 0.5$. Besides the waveforms observed in several fundamental cycles of v_C, which describe the slow-scale dynamic behaviors of the inverter, the magnified waveforms of v_C and i_o in successive switching cycles are also provided to present the fast-scale dynamic behaviors of the inverter. Obviously, the magnified waveforms demonstrate almost the same stability characteristics as the normal waveforms, and that means the fast- and slow-scale stability are consistent for the inverter under resistive load condition, which is also consistent with the theoretical results.

The transient waveforms under resistive load condition when $k_i = 20$, $K = 0.5$, and $k_p = 0.04$ are presented in Fig. 17, including the transient waveforms in response to no load to nominal resistive load step change, and transient waveforms in response to +50% step change of load resistor. Clearly, the transient waveforms prove that the dynamic response of the PWM inverter with resistive load is quite fast.

Fig. 18 illustrates the steady-state waveforms under resistive load condition for different *K* when $k_i = 20$ and $k_p = 0.04$. As shown in Fig. 18, waveforms of the filter capacitor voltage v_C and output current i_o are periodic and sinusoidal without any distortion when $K = 0.542$, which indicates that the PWM inverter is stable. When $K = 0.642$, waveforms of v_C and i_o become slightly distorted, which means that the PWM inverter is nearly critically stable. And when *K* increases to 0.742, noticeable oscillation is observed in the waveforms, which indicates that the PWM inverter becomes unstable. And when $K = 0.842$, significant oscillation appears in waveforms of v_C and i_o, and that means the PWM inverter is highly unstable in this case. Thus, the experimental results in Fig. 18 show consistency with the theoretical results, i.e., the PWM inverter becomes unstable when $K > 0.742$ for $k_i = 20$ and $k_p = 0.04$. In addition, the presented magnified waveforms of v_C and i_o also show similar dynamic properties like those in the normal waveforms, and verify the consistency of the fast- and slow-scale stability for the PWM inverter.

B. Experimental Results Under Inductive–Resistive Load Condition

The steady-state waveforms under inductive–resistive load condition for different k_p when $k_i = 20$ and $K = 0.5$ are shown in Fig. 19. It can be seen that, waveforms of filter capacitor voltage v_C and output current i_o are sinusoidal and periodic when $k_p = 0.05$, which indicates that the PWM inverter is stable. But when $k_p = 0.06$, waveforms of v_C and i_o become slightly distorted, which means that the PWM inverter is almost critically stable. And when $k_p = 0.07$, waveforms of v_C and i_o become oscillating, which means that the PWM inverter becomes unstable. When $k_p = 0.08$, waveforms of v_C and i_o oscillate remarkably, which indicates that the PWM inverter is totally unstable.

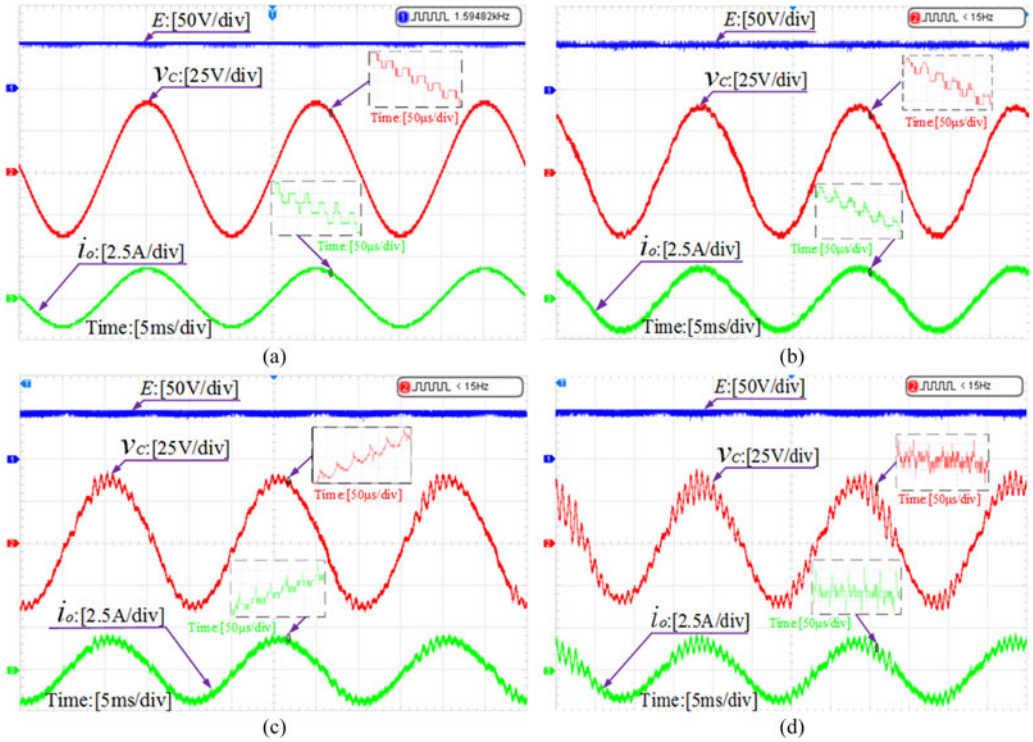

Fig. 16. Steady-state waveforms under resistive load condition for different k_p when $k_i = 20$ and $K = 0.5$. (a) $k_p = 0.042$; (b) $k_p = 0.062$; (c) $k_p = 0.082$; (d) $k_p = 0.102$.

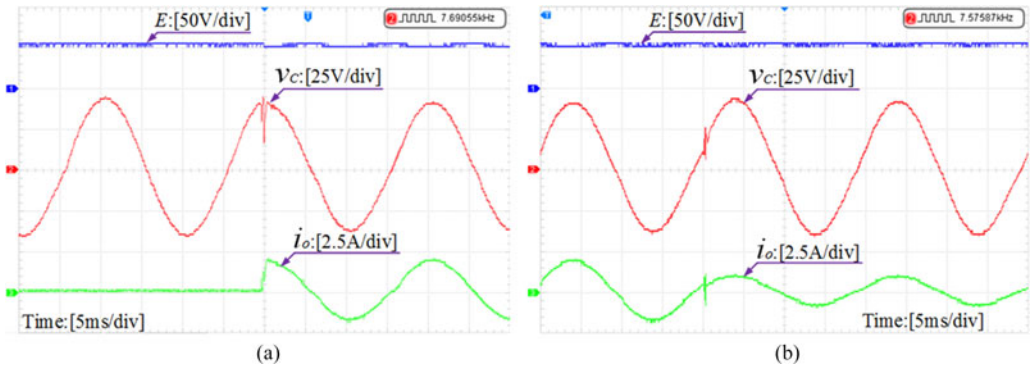

Fig. 17. Transient waveforms under resistive load condition when $k_i = 20$, $K = 0.5$, and $k_p = 0.04$. (a) Transient waveforms in response to no load to nominal resistive load step change; (b) transient waveforms in response to $+50\%$ step change of load resistor.

Thus, the experimental results in Fig. 19 show good conformity with the theoretical result that the PWM inverter becomes unstable when $k_p > 0.07$ for $k_i = 20$ and $K = 0.5$. Furthermore, as can be observed in Fig. 19, the magnified and normal waveforms of v_C and i_o are also substantially consistent in dynamic characteristics, which proves the concordance of the fast- and slow-scale stability for the inverter under inductive–resistive load condition.

Fig. 20 depicts the transient waveforms under inductive–resistive load condition when $k_i = 20$, $K = 0.5$, and $k_p = 0.04$, including both the transient waveforms in response to no load to nominal resistive load step change, and transient waveforms in response to -50% step change of load resistor. It can be seen that the dynamic performance of the PWM inverter with inductive–resistive load is also excellent.

C. Experimental Results Under Nonlinear Load Condition

Fig. 21 presents the steady-state waveforms under nonlinear load condition with and without using harmonic control scheme for the 3rd, 5th, 7th, 9th, and 11th harmonic components. As shown in Fig. 21(b), by employing the harmonic control scheme, the 3rd, 5th, 7th, 9th, and 11th harmonic components are significantly reduced. The total harmonic distribution (THD) of v_C becomes smaller, and approximately sinusoidal waveform of v_C is obtained, which validates the effectiveness of the proposed harmonic control scheme.

The steady-state waveforms under nonlinear load condition for different k_p when $k_i = 20$ and $K = 0.5$ are shown in Fig. 22. In Fig. 22(a), when $k_p = 0.038$ which is lower than the critical value 0.048 in Fig. 11, the THD of v_C is relatively small. But when k_p increases to 0.058, the THD of v_C becomes much

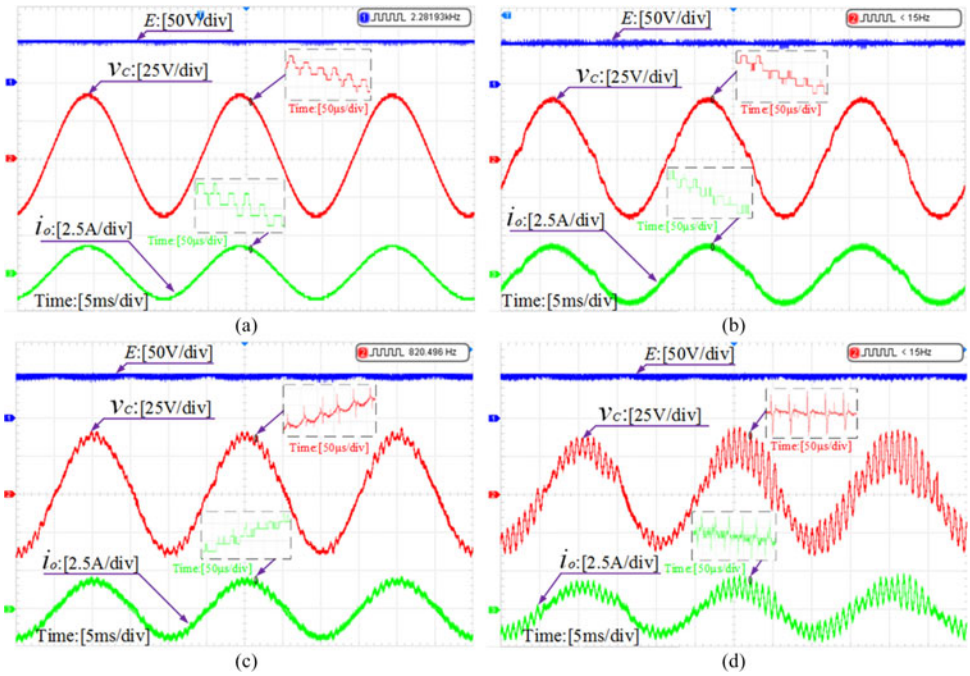

Fig. 18. Steady-state waveforms under resistive load condition for different K when $k_i = 20$ and $k_p = 0.04$. (a) $K = 0.542$; (b) $K = 0.642$; (c) $K = 0.742$; (d) $K = 0.842$.

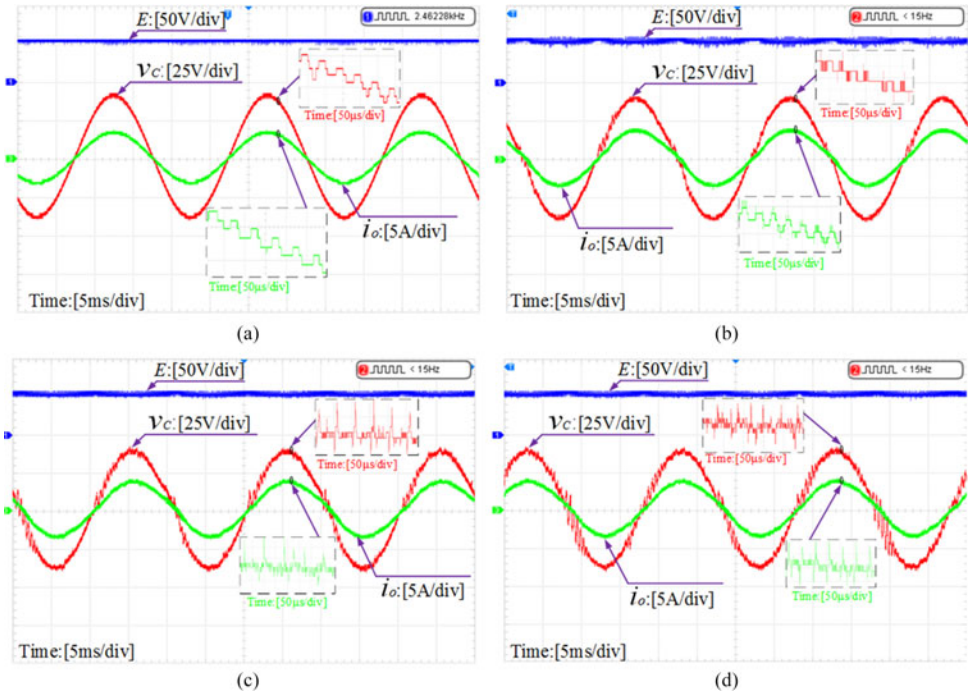

Fig. 19. Steady-state waveforms under inductive–resistive load condition for different k_p when $k_i = 20$, $K = 0.5$. (a) $k_p = 0.05$; (b) $k_p = 0.06$; (c) $k_p = 0.07$; (d) $k_p = 0.08$.

higher, as shown in Fig. 22(b). The experimental results reveal that, the Lyapunov exponent method and equivalent model of diode rectifier are effective for the approximate slow-scale stability analysis under nonlinear load condition.

Fig. 23 demonstrates the steady-state waveforms under nonlinear load condition for different K when $k_i = 20$ and $k_p = 0.04$. It can be seen that, when $K = 0.452$ which is lower than the critical value 0.552 in Fig. 15, the harmonic distortion of v_C is less obvious. However, when $K = 0.652$ which is higher than 0.552, the harmonic distortion of v_C increases significantly, as shown in Fig. 23(b). The experimental results also clearly verify the validity of the Lyapunov exponent method and equivalent model of diode rectifier for the approximate slow-scale stability analysis under nonlinear load condition.

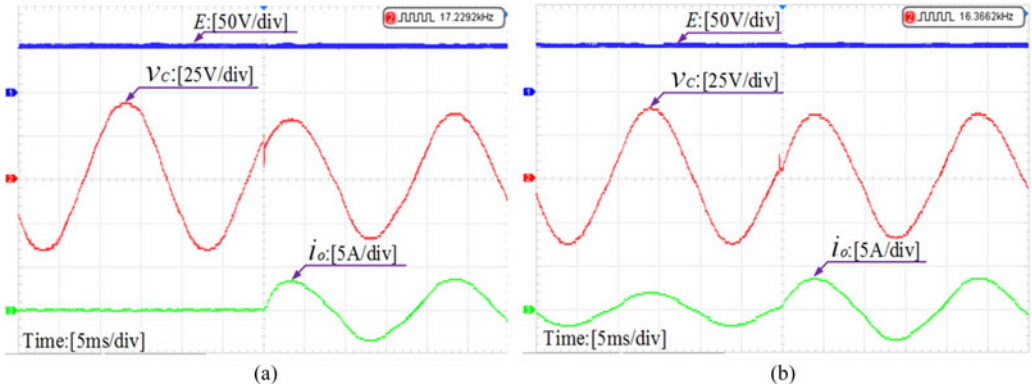

Fig. 20. Transient waveforms under inductive–resistive load condition when $k_i = 20$, $K = 0.5$, and $k_p = 0.04$. (a) Transient waveforms in response to no load to nominal resistive load step change; (b) transient waveforms in response to -50% step change of load resistor.

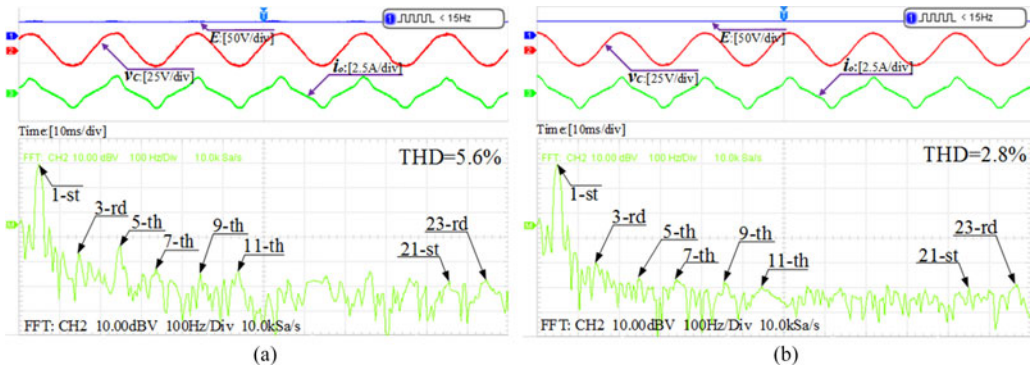

Fig. 21. Steady-state waveforms under nonlinear load condition with and without using harmonic control scheme. (a) Without using harmonic control scheme. (b) With using harmonic control scheme.

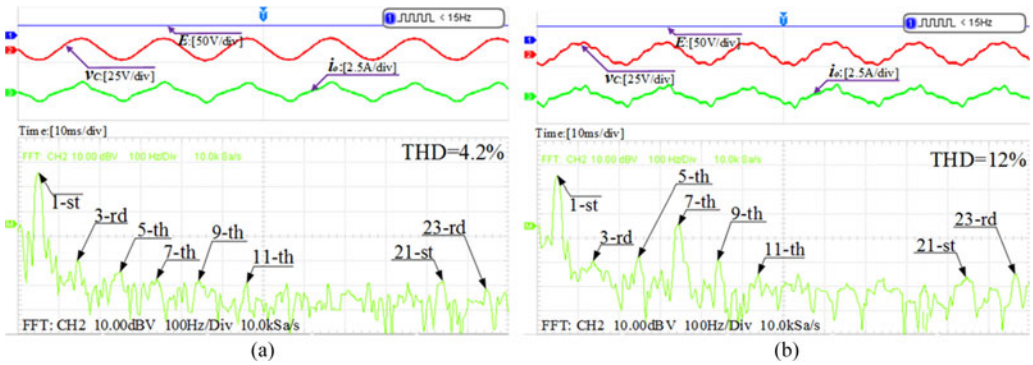

Fig. 22. Steady-state waveforms under nonlinear load condition for different k_p when $k_i = 20$ and $K = 0.5$ for different k_p. (a) $k_p = 0.038$. (b) $k_p = 0.058$.

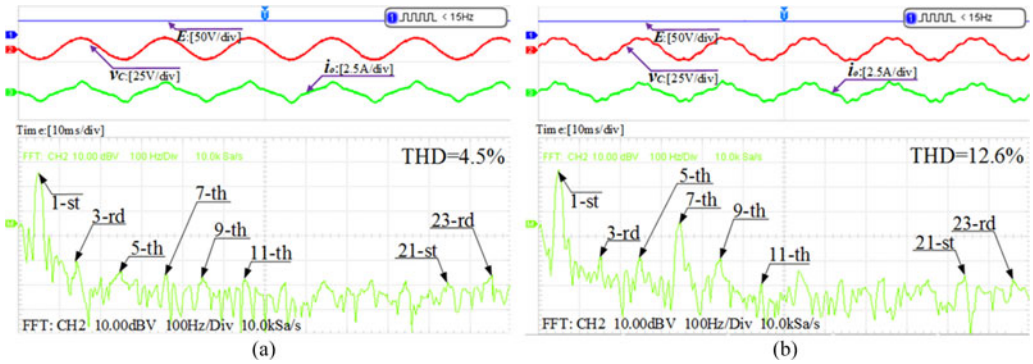

Fig. 23. Steady-state waveforms under nonlinear load condition for different *K* when $k_i = 20$ and $k_p = 0.04$ for different *K*. (a) $K = 0.452$. (b) $K = 0.652$.

VI. Conclusion

This paper presents the stability analysis of a digital-controlled single-phase VSI with SRF voltage control by employing two nonlinear approaches, the Jacobian matrix method and the Lyapunov exponent method. To adopt these two methods, the stroboscopic model of the PWM inverter is established by using the SSA technique. The analyses are subsequently implemented under variations of three control parameters of voltage loop and current loop, and stability regions of the PWM inverter system are obtained.

In addition, for the derived stroboscopic model, the Jacobian matrix method and the Lyapunov exponent method are proved to be mathematically equivalent. Therefore, the fast-scale stability and slow-scale stability described by the Jacobian matrix method and the Lyapunov exponent method respectively are consistent for the studied PWM inverter in stand-alone mode. The theoretical results are verified by the experimental results, which indicates that discrete-time model plus the Jacobian matrix method or the Lyapunov exponent method are capable to analyze the stability of a switching converter with SRF control loops accurately.

Appendix A

Expressions of α, β, K_1, K_2, K_3, K_4 in (5)

$$\alpha = -\frac{1}{2RC} \tag{A1}$$

$$\beta = \sqrt{\frac{1}{LC} - \frac{1}{(2RC)^2}} \tag{A2}$$

$$K_1 = i_L(n) + \frac{1}{R}[1-2d(n)]E \tag{A3}$$

$$K_2 = -\frac{v_C(n) + [1-2d(n)]E}{\beta L} - \frac{\alpha}{\beta R}\{Ri_L(n) + [1-2d(n)]E\} \tag{A4}$$

$$K_3 = v_C(n) + [1-2d(n)]E \tag{A5}$$

$$K_4 = \left(\frac{\alpha^2 L}{\beta} + \beta L\right) i_L(n) + \frac{\alpha}{\beta} v_C(n) + \frac{\alpha R + \alpha^2 L + \beta^2 L}{\beta R}[1-2d(n)]E. \tag{A6}$$

Appendix B

Definitions of coefficients in (8)

$$r = \sqrt[3]{-\frac{q}{2} + \sqrt{\frac{q^2}{4} + \frac{p^3}{27}}} + \sqrt[3]{-\frac{q}{2} - \sqrt{\frac{q^2}{4} + \frac{p^3}{27}}} - \frac{R_1}{3L_1} \tag{B1}$$

$$\alpha_1 = -\frac{1}{2}\left(\sqrt[3]{-\frac{q}{2} + \sqrt{\frac{q^2}{4} + \frac{p^3}{27}}} + \sqrt[3]{-\frac{q}{2} - \sqrt{\frac{q^2}{4} + \frac{p^3}{27}}}\right) - \frac{R_1}{3L_1} \tag{B2}$$

$$\beta_1 = \frac{\sqrt{3}}{2}\left(\sqrt[3]{-\frac{q}{2} + \sqrt{\frac{q^2}{4} + \frac{p^3}{27}}} - \sqrt[3]{-\frac{q}{2} - \sqrt{\frac{q^2}{4} + \frac{p^3}{27}}}\right) \tag{B3}$$

$$p = \frac{L + L_1}{LL_1C} - \frac{R_1^2}{3L_1^2} \tag{B4}$$

$$q = \frac{R_1}{LL_1C} - \frac{2R_1^3}{27L_1^3} - \frac{R_1(L+L_1)}{3LL_1^2C} \tag{B5}$$

$$K_5 = \left[-\frac{1}{\theta LC} + \frac{\beta_1^2 - \alpha_1^2}{\theta} - \frac{\alpha_1 L}{\theta}\right] i_L(n) - \frac{2\alpha_1}{\theta L} v_C(n) + \frac{1}{\theta LC} i_o(n) - \frac{2\alpha_1[2d(n)-1]E}{\theta L} \tag{B6}$$

$$K_6 = i_L(n) - K_5 \tag{B7}$$

$$K_7 = \frac{1}{L\beta_1}\{[2d(n)-1]E - v_C(n) - \alpha_1 L i_L(n)\} - \frac{r-\alpha_1}{\beta_1} K_5 \tag{B8}$$

$$\theta = r^2 - 2\alpha_1 + \alpha_1^2 - \beta_1^2. \tag{B9}$$

Appendix C

Expressions of matrix elements in (13)

$$\frac{\partial i_L(n+1)}{\partial i_L(n)} = e^{\alpha T}\left(\cos\beta T - \frac{\alpha}{\beta}\sin\beta T\right) \tag{C1}$$

$$\frac{\partial i_L(n+1)}{\partial v_C(n)} = -\frac{1}{\beta L} e^{\alpha T}\sin\beta T \tag{C2}$$

$$\frac{\partial i_L(n+1)}{\partial d(n)} = \frac{2E}{R}\left[e^{\alpha T}\left(\frac{\alpha L + R}{\beta L}\sin\beta T - \cos\beta T\right) + 1\right] \tag{C3}$$

$$\frac{\partial v_C(n+1)}{\partial i_L(n)} = \frac{\alpha^2 L + \beta^2 L}{\beta} e^{\alpha T}\sin\beta T \tag{C4}$$

$$\frac{\partial v_C(n+1)}{\partial v_C(n)} = e^{\alpha T}\left(\cos\beta T + \frac{\alpha}{\beta}\sin\beta T\right) \tag{C5}$$

$$\frac{\partial v_C(n+1)}{\partial d(n)} = 2E\left[1 - e^{\alpha T}\left(\cos\beta T + \frac{\alpha R + \alpha^2 L + \beta^2 L}{\beta R}\sin\beta T\right)\right] \tag{C6}$$

$$\frac{\partial d(n+1)}{\partial i_L(n)} = -\frac{1}{2}K \tag{C7}$$

$$\frac{\partial d(n+1)}{\partial v_C(n)} = \frac{1}{2}K\left(\frac{1}{R} - k_p - k_i T\right) \tag{C8}$$

$$\frac{\partial d(n+1)}{\partial d(n)} = 0. \tag{C9}$$

Reference

[1] M. Castilla, J. Miret, J. Matas, L. G. de Vicuña, and J. M. Guerrero, "Control design guidelines for single-phase grid-connected photovoltaic inverters with damped resonant harmonic compensators," *IEEE Trans. Ind. Electron.*, vol. 56, no. 11, pp. 4492–4501, Nov. 2009.

[2] D. Dong *et al.*, "Modes of operation and system-level control of single-phase bidirectional pwm converter for microgrid systems," *IEEE Trans. Smat Grid.*, vol. 3, no. 1, pp. 93–104, Mar. 2012.

[3] R. J. Wai, C. Y. Lin, Y. C. Huang, and Y. R. Chang, "Design of high-perform -ance stand-alone and grid-connected inverter for distributed generation applications," *IEEE Trans. Ind. Electron.*, vol. 60, no. 4, pp. 1542–1555, Apr. 2013.

[4] C. Trujillo, D. Velasco, G. Garcera, E. Figueres, and J. Guacaneme, "Reconfig-urable control scheme for a PV microinverter working in both grid-connected and island modes," *IEEE Trans. Ind. Electron.*, vol. 60, no. 4, pp. 1582–1595, Apr. 2013.

[5] B. Bhandari, K.-T. Lee, C. S. Lee, C.-K. Song, R. K. Maskey, and S.-H. Ahn, "A novel off-grid hybrid power system comprised of solar photo-voltaic,wind, and hydro energy sources," *Appl. Energy*, vol. 133, no. 10, pp. 236–242, Aug. 2014.

[6] H. Deng, R. Oruganti, and D. Srinivasan, "A simple control method for high-performance UPS inverters through output-impedance reduction," *IEEE Trans. Ind. Electron.*, vol. 55, no. 02, pp. 888–898, Feb. 2008.

[7] X. Zhang and J. W. Spencer, "Study of multisampled multilevel inverters to improve control performance," *IEEE Trans. Power Electron.*, vol. 27, no. 11, pp. 4409–4416, Jan. 2012.

[8] P. Mattavelli, "An improved deadbeat control for UPS using disturbance observers," *IEEE Trans. Ind. Electron.*, vol. 52, no. 1, pp. 206–212, Feb. 2005.

[9] W. S. Song, J. P. Ma, L. Zhou, and X. Y. Feng, "Deadbeat predictive power control of single-phase three-level neutral-point-clamped converters using space-vector modulation for electric railway traction," *IEEE Trans. Power Electron.*, vol. 31, no. 01, pp. 721–732, Jan. 2016.

[10] K. Zhang, Y. Kang, J. Xiong, and J. Chen, "Direct repetitive control of SPWM inverter for UPS purpose," *IEEE Trans. Power Electron.*, vol. 18, no. 3, pp. 784–792, May 2003.

[11] K. Zhou, K. Low, D. Wang, F. Luo, B. Zhang, and Y. Wang, "Zero-phase odd-harmonic repetitive controller for a single-phase PWM inverter," *IEEE Trans. Power Electron.*, vol. 21, no. 1, pp. 193–201, Jan. 2006.

[12] O. Kukrer, H. Komurcugil, and A. Doganalp, "A three-level hysteresis function approach to the sliding-mode control of single-phase UPS inverters," *IEEE Trans. Ind. Electron.*, vol. 56, no. 9, pp. 3477–3486, Sep. 2009.

[13] H. Komurcugil, "Rotating-sliding-line-based sliding-mode control for single-phase UPS inverters," *IEEE Trans. Ind. Electron.*, vol. 59, no. 10, pp. 3719–3726, Oct. 2012.

[14] G. Bonan, O. Mano, L. F. A. Pereira, and D. F. Coutinho, "Robust control design of multiple resonant controllers for sinusoidal tracking and harmonic rejection in uninterruptible power supplies," in *Proc. IEEE ISIE*, Jul. 2010, pp. 303–308.

[15] S. A. Khajehoddin, M. Karimi-Ghartemani, P. K. Jain, and A. Bakhshai, "A resonant controller with high structural robustness for fixed-point digital implementations," *IEEE Trans. Power Electron.*, vol. 27, no. 7, pp. 3352–3362, Jul. 2012.

[16] M. Cespedes and J. Sun, "Adaptive control of grid-connected inverters based on online grid impedance measurements," *IEEE Trans. Sustain. Energy*, vol. 05, no. 02, pp. 516–523, Apr. 2014.

[17] X. Fu and S. Li, "Control of single-phase grid-connected converters with *LCL* filters using recurrent neural network and conventional control methods," *IEEE Trans. Power Electron.*, vol. 31, no. 07, pp. 5354–5364, Jul. 2016.

[18] E. D. Bolat and H. M. Ertunç, "Control of single phase UPS inverter using fuzzy gain scheduling of PI controller," in *Proc. ELECO*, Sep. 2011, pp. I-381–I-385.

[19] M. J. Ryan and R. D. Lorenz, "A synchronous-frame controller for a single-phase sine wave inverter," in *Proc. IEEE APEC*, Feb. 1997, pp. 813–819.

[20] A. Roshan, R. Burgos, A. C. Baisden, F. Wang, and D. Boroyevich, "A D-Q frame controller for a full-bridge single phase inverter usedin small distributed power generation systems," in *Proc. IEEE APEC*, Feb. 2007, pp. 641–647.

[21] B. Bahrani, A. Rufer, S. Kenzelmann, and L. Lopes, "Vector control of single-phase voltage source converters based on fictive axis emulation," *IEEE Trans. Ind. Appl.*, vol. 47, no. 2, pp. 831–840, Mar./Apr. 2011.

[22] D. Dong, T. Thacker, R. Burgos, F. Wang, and D. Boroyevich, "On zero steady-state error voltage control of single-phase PWM inverters with different load types," *IEEE Trans. Power Electron.*, vol. 26, no. 11, pp. 3285–3297, Nov. 2011.

[23] M. Monfared, S. Golestan, and J. M. Guerrero, "Analysis, design, and experimental verification of a synchronous reference frame voltage control for single-phase inverters," *IEEE Trans. Ind. Electron.*, vol. 61, no. 1, pp. 258–269, Jan. 2014.

[24] X. Wu, G. Xiao, and B. Lei, "Simplified discrete-time modeling for convenient stability prediction and digital control design," *IEEE Trans. Power Electron.*, vol. 28, no. 11, pp. 5333–5342, Nov. 2013.

[25] X. Wu, G. Xiao, Y. Lu, F. Chen, and D. Lu, "Discrete-time modeling and stability analysis of grid-connected inverter based on equivalent circuit," in *Proc. IEEE Appl. Power Electron. Conf. Expo.*, 2015, pp. 1222–1226.

[26] D. C. Hamill, J. H. B. Deane, and D. J. Jefferies, "Modeling of chaotic DC–DC converters by iterated nonlinear mappings," *IEEE Trans. Ind. Electron.*, vol. 7, no. 1, pp. 25–36, Jan. 1992.

[27] J. H. B. Deane, "Chaos in a current-mode controlled boost dc-dc convert," *IEEE Trans. Circuits Syst. I, Reg. Papers*, vol. 39, no. 8, pp. 680–683, Aug. 1992.

[28] K. Chakrabarty, G. Poddar, and S. Banerjee, "Bifurcation behavior of the buck converter," *IEEE Trans. Ind. Electron.*, vol. 11, no. 3, pp. 439–447, May 1996.

[29] H. H. C. Iu and B. Robert, "Control of chaos in a PWM current-mode h-bridge inverter using time-delayed feedback," *IEEE Trans. Circuits Syst. I, Reg. Papers*, vol. 50, no. 8, pp. 1125–1129, Aug. 2003.

[30] H. Komurcugil, N. Altin, S. Ozdemir, and I. Sefa, "An extended Lyapunov-function-based control strategy for single-phase UPS inverters," *IEEE Trans. Power Electron.*, vol. 30, no. 7, pp. 3976–3983, Jul. 2015.

[31] H. Komurcugil, "Steady-state analysis and passivity-based control of single-phase PWM current-source inverters," *IEEE Trans. Ind. Electron.*, vol. 57, no. 3, pp. 1026–1030, Mar. 2010.

[32] C. Meza, D. Biel, D. Jeltsema, and J. M. A. Scherpen, "Lyapunov based control scheme for single phase grid-connected PV central inverters," *IEEE Trans. Control Syst. Technol.*, vol. 20, no. 2, pp. 520–529, Mar. 2012.

[33] H. Komurcugil, N. Altin, S. Ozdemir, and I. Sefa, "Lyapunov-function and proportional-resonant based control strategy for single-phase grid-connected VSI with *LCL* filter," *IEEE Trans. Ind. Electron.*, vol. 63, no. 5, pp. 2838–2849, May 2016.

[34] M. Rezkallah, S. Sharma, A. Chandra, B. Singh, and D. R. Rousse, "Lyapunov function and sliding mode control approach for solar-PV grid interface system," *IEEE Trans. Ind. Electron.*, vol. 64, no. 1, pp. 785–795, Jan. 2017.

[35] X. Wu, C. K. Tse, O. Dranga, and J. Lu, "Fast-scale instability of single-stage power-factor-correction power supplies," *IEEE Trans. Circuits Syst. I, Reg. Papers*, vol. 53, no. 1, pp. 204–213, Jan. 2006.

[36] D. Giaouris, S. Banerjee, B. Zahawi, and V. Pickert, "Control of fast scale bifurcations in power-factor correction converters," *IEEE Trans. Circuits Syst. II, Exp. Briefs*, vol. 54, no. 9, pp. 805–809, Sep. 2007.

[37] Alan Wolf, J. B. Swift, H. L. Swinney, and J. A. Vastano, "Determining lyapunov exponents from a time series," *Physica D*, vol. 16, no. 3, pp. 285–317, Jul. 1985.

[38] L.-M. Saublet, G.-G. Roghayeh, J.-P. Martin, N.-M. Babak, and S. Pierfederici, "Asymptotic stability analysis of the limit cycle of a cascaded DC–DC converter using sampled discrete-time modeling," *IEEE Trans. Ind. Electron.*, vol. 63, no. 4, pp. 2477–2487, Apr. 2016.

[39] H. K. Khalil, *Nonlinear Systems*, 2nd ed. Englewood Cliffs, NJ, USA: Prentice-Hall, 1996.

[40] C. K. Tse, *Complex Behavior of Switching Power Converters*, 1st ed. Boca Raton, FL, USA: CRC Press, 2004.

[41] X. Zhang, J. Xu, B. Bao, and G. Zhou, "Asynchronous-switching map-based stability effects of circuit parameters in fixed off-time controlled buck converter," *IEEE Trans. Power Electron.*, vol. 31, no. 9, pp. 6686–6697, Sep. 2016.

[42] M. di Bernardo and F. Vasca, "Discrete-time maps for the analysis of bifurcations and chaos in DC/DC converters," *IEEE Trans. Power Electron.*, vol. 47, no. 02, pp. 130–143, Feb. 2000.

[43] R. D. Middlebrook and S. Cuk, "A general unified approach to modeling switching power converter stages," in *Proc. IEEE Power Electron. Spec. Conf. Rec.*, 1976, pp. 18–34.

[44] A. Mansoor, W. M. Grady, A. H. Chowdhury, and M. J. Samotyj, "An investigation of harmonics attenuation and diversity among distributed single-phase power electronic loads," *IEEE Trans. Power Del.*, vol. 10, no. 1, pp. 467–473, Jan. 1995.

[45] D.-G. Kim, T. Nakajima, Nonmembers, and E. Masada, "Harmonic analysis of a capacitor-filtered rectifier with line impedance," *Electron. Commun. Japan Part I, Commun.*, vol. 72, no. 4, pp. 1–9, Apr. 1989.

[46] M. Chen, C. Zheng, Z. Qian, and X. Yuan, "The analysis of inverter under rectifier load using a nonlinear rectifier model," in *Proc. INTELEC*, Sep. 2005, vol. 28, no. 15, pp. 455–459.

Yang Han (S'08–M'10–SM'17) received the Ph.D. in electrical engineering from Shanghai JiaoTong University (SJTU), Shanghai, China, in 2010.

In 2010, he joined the Department of Power Electronics, School of Mechatronics Engineering, University of Electronic Science and Technology of China (UESTC), Chengdu, China, where he has been an Associate Professor since 2013. From March 2014 to March 2015, he was a Visiting Scholar (Guest Postdoc) in the Department of Energy Technology, Aalborg University, Aalborg, Denmark. His current research interests include ac/dc microgrids, grid-connected converters for renewable energy systems and DGs, power quality, active power filters, and static synchronous compensators (STATCOMs). He has 10 issued and 13 pending patents.

Dr. Han was the Session Chair in "Power Quality Mitigation and Application" in the Fifth National Conference on Power Quality in Xi'an in 2017 and the Session Chair in "AC/DC, DC/AC Power Converter" session in the 2016 IPEMC ECCE-Asia in Hefei, China. He received the "Baekhyun Award" by the Korean Institute of Power Electronics (KIPE) in 2016. He received the Best Paper Awards from the Fifth National Conference on Power Quality in 2017, the Annual Conference of HVDC and Power Electronics Committee of the Chinese Society of Electrical Engineers (CSEE) in 2013, and the Fourth International Conference on Power Quality in 2008, China.

Xu Fang received the B.S. degree in electrical engineering and automation in 2015 from the University of Electronic Science and Technology of China (UESTC), Chengdu, China, where he is currently working toward the M.S. degree in power electronics and electric drives.

His current research interests include system modeling and stability analysis of power electronic converters and microgids, power quality management, and control methods of distributed generation systems.

Ping Yang received the B.S. in mechanical engineering from Shanghai JiaoTong University (SJTU), Shanghai, China, in 1984, and the M.S. degree in mechanical engineering from Sichuan University, Sichuan, China, in 1987.

He is currently a Full Professor with the School of Mechatronics Engineering, University of Electronic Science and Technology of China (UESTC), Chengdu, China. He was visiting the Victory University, Australia, from July 2004 to August 2004, and a Visiting Scholar with the S. M. Wu Manufacturing Research Center, University of Michigan, Ann Arbor, MI, USA, from August 2009 to February 2010, and was visiting the University of California, Irvine, CA, USA, from October 2012 to November 2012. His current research includes mechatronics engineering, electrical engineering and automation, computer-aided control and instrumentation, smart mechatronics, and detection and automation of mechanical equipment. He has authored more than 60 papers in various journals and international conferences and several books on mechatronics and instrumentation. He is currently the Dean of the School of Mechatronics Engineering, UESTC.

Prof. Yang has received several provincial awards for his contribution in teaching and academic research.

Congling Wang received the B.S. degree from Nanjing University of Aeronautics and Astronautics, Nanjing, China, in 1991, and the M.S. degree from the University of Electronic Science and Technology of China (UESTC), Chengdu, China, in 1996.

Since 1996, he has been a Faculty Member of the School of Mechatronics Engineering, UESTC, where he is currently an Associate Professor. His current research interests include the mechatronics engineering, electrical engineering and automation, computer-aided control and instrumentation, smart mechatronics, and detection and automation of mechanical equipment.

Lin Xu received the Ph.D. degree in electrical engineering from Shanghai JiaoTong University (SJTU), Shanghai, China, in 2011.

She is currently a Senior Engineering at Sichuan Electric Power Research Institute, State Grid Sichuan Electric Power Company, Chengdu, China. She has coauthored more than 20 journal and conference papers in the area of power electronics and power systems. Her current research interests include power quality, power system analysis and real-time digital simulator (RTDS), and flexible ac transmission systems (FACTS), such as STATCOMs and power quality conditioners (DVRs, APFs). She is an active Reviewer for the *Electric Power Components and Systems*, etc.

Dr. Xu is an active Reviewer for the IEEE TRANSACTIONS ON INDUSTRIAL ELECTRONICS and the IEEE TRANSACTIONS ON POWER ELECTRONICS.

Josep M. Guerrero (S'01–M'04–SM'08–FM'15) received the B.S. degree in telecommunications engineering, the M.S. degree in electronics engineering, and the Ph.D. degree in power electronics from the Technical University of Catalonia, Barcelona, Spain, in 1997, 2000, and 2003, respectively.

Since 2011, he has been a Full Professor with the Department of Energy Technology, Aalborg University, Aalborg, Denmark, where he is responsible for the Microgrid Research Program. In 2012, he was a Guest Professor at the Chinese Academy of Science and the Nanjing University of Aeronautics and Astronautics; in 2014, he was the Chair Professor at Shandong University; in 2015, he was a Distinguished Guest Professor at Hunan University; and in 2016, he was a Visiting Professor Fellow at Aston University, U.K. His current research interests include different microgrid aspects, including power electronics, distributed energy-storage systems, hierarchical and cooperative control, energy management systems, smart metering and the internet of things for ac/dc microgrid clusters, and islanded minigrids; recently, specially focused on maritime microgrids for electrical ships, vessels, ferries and seaports.

Prof. Guerrero is an Associate Editor for the IEEE TRANSACTIONS ON POWER ELECTRONICS, the IEEE TRANSACTIONS ON INDUSTRIAL ELECTRONICS, and the IEEE INDUSTRIAL ELECTRONICS MAGAZINE, and an Editor for the IEEE TRANSACTIONS ON SMART GRID and the IEEE TRANSACTIONS ON ENERGY CONVERSION. He has been a Guest Editor of the IEEE TRANSACTIONS ON POWER ELECTRONICS SPECIAL ISSUES: POWER ELECTRONICS FOR WIND ENERGY CONVERSION AND POWER ELECTRONICS FOR MICROGRIDS; the IEEE TRANSACTIONS ON INDUSTRIAL ELECTRONICS SPECIAL SECTIONS: UNINTERRUPTIBLE POWER SUPPLIES SYSTEMS, RENEWABLE ENERGY SYSTEMS, DISTRIBUTED GENERATION AND MICROGRIDS, AND INDUSTRIAL APPLICATIONS AND IMPLEMENTATION ISSUES OF THE KALMAN FILTER; the IEEE TRANSACTIONS ON SMART GRID SPECIAL ISSUES: SMART DC DISTRIBUTION SYSTEMS AND POWER QUALITY IN SMART GRIDS; the IEEE TRANSACTIONS ON ENERGY CONVERSION SPECIAL ISSUE ON ENERGY CONVERSION IN NEXT-GENERATION ELECTRIC SHIPS. He was the Chair of the Renewable Energy Systems Technical Committee of the IEEE Industrial Electronics Society. He received the best paper award of the IEEE Transactions on Energy Conversion for the period 2014–2015. In 2014 and 2015, he was awarded by Thomson Reuters as Highly Cited Researcher, and in 2015, he was elevated as IEEE Fellow for his contributions on "distributed power systems and microgrids."